JOURNAL OF GUIDANCE, CONTROL, AND DYNAMICS
Vol. 31, No. 4, July–August 2008

Structured Adaptive Model Inversion Controller for Mars Atmospheric Flight

Carolina Restrepo* and John Valasek†
Texas A&M University, College Station, Texas 77843

DOI: 10.2514/1.33085

The new vision for manned Mars exploration presents challenges that are critically different from past experiences with robotic missions. Safe precision landing requirements for manned missions make it necessary to fly a controlled entry trajectory, rather than the more robust ballistic entry trajectory traditionally used for robotic missions. Large variations and uncertainties in Mars atmospheric properties also pose a significant challenge. Model reference adaptive control has not been previously used for Mars entry control, but it is an attractive candidate. It has an adaptation mechanism that reduces tracking errors in the presence of uncertain parameters such as atmospheric density and vehicle properties such as aerodynamic coefficients and inertias. This paper develops and implements two different model reference adaptive control schemes for the Mars ellipsled vehicle and evaluates them with non-real-time simulation for a complete Mars entry trajectory-tracking scenario from entry interface to parachute deployment. Performance metrics are introduced, and the relative benefits and disadvantages of each controller are discussed. Each controller is evaluated in terms of trajectory-tracking performance while in the presence of uncertainties in the atmospheric density, uncertainties in the aerodynamic coefficients, and uncertainties in the vehicle inertias. Results presented in the paper demonstrate that the learning rates for both controllers can be tuned to obtain acceptable tracking performance during an entire entry trajectory. Which of the two model reference adaptive controllers is most suitable for a particular Mars entry application depends upon the tradeoff between level of performance and higher control effort and on the level of difficulty in the synthesis and implementation efforts.

Nomenclature

C_D	=	drag coefficient
C_L	=	lift coefficient
C_{l_β}	=	rolling-moment stability derivative
C_{m_α}	=	pitching-moment stability derivative
C_{n_β}	=	yawing-moment stability derivative
$\mathbf{D}$	=	drag vector
G	=	known parameter vector for the structured adaptive model inversion controller
$\mathbf{g}$	=	Mars gravity
h	=	altitude
I	=	inertia matrix
$\mathbf{L}$	=	lift vector
$\mathcal{L}$	=	rolling moment
L	=	unknown parameter vector for the structured adaptive model inversion controller
l_{ref}	=	reference length
$\mathcal{M}$	=	pitching moment
$\mathcal{N}$	=	yawing moment
p	=	roll rate
q	=	pitch rate
$\mathbf{q}$	=	classical Rodrigues parameter vector
r	=	yaw rate
S_{ref}	=	reference area
$\mathbf{u}$	=	control input vector
V	=	Lyapunov function
$\mathbf{v}$	=	velocity vector
x_{cg}	=	center-of-gravity x coordinate
y_{cg}	=	center-of-gravity y coordinate
z_{cg}	=	center-of-gravity z coordinate
α	=	angle of attack
β	=	sideslip angle
Γ	=	learning rate
γ	=	flight-path angle

Carolina Restrepo earned a B.S. Magna Cum Laude (2005) and M.S. (2007) in aerospace engineering from Texas A&M University. She is a recipient of the National Science Foundation Graduate Research Fellowship and the Texas Space Grant Consortium Fellowship. From 2003–2008 she served six Co-Op tours at the NASA Johnson Space Center, the last four of which were in the Aeroscience and Flight Mechanics Division. For her efforts, she was twice awarded the NASA Johnson Space Center Outstanding Co-Op Award. From 2005 to 2007 she was a Graduate Research Assistant in the Aerospace Engineering Department at Texas A&M University, where she researched nonlinear adaptive control for Mars entry vehicles as part of her M.S. research. She is currently pursuing a Ph.D. in aerospace engineering at Texas A&M University. She is a Member of AIAA.

A biography of John Valasek appears in Vol. 29, No. 4.

Presented as Paper 6850 at the AIAA Guidance, Navigation, and Control Conference, Hilton Head, SC, 20–23 August 2007; received 26 June 2007; revision received 10 February 2008; accepted for publication 15 February 2008.

*Graduate Research Assistant, Vehicle Systems and Control Laboratory, Aerospace Engineering Department; caro@tamu.edu. Member AIAA.
†Associate Professor and Director, Vehicle Systems and Control Laboratory, Aerospace Engineering Department; valasek@tamu.edu. Associate Fellow AIAA.

ξ = heading angle
ρ = Mars atmospheric density
Φ = roll angle
ϕ = bank angle
Ψ = yaw angle
ω = angular velocity

Subscripts

m = model
p = plant
r = reference signal
ω = plant angular velocity

Superscripts

$*$ = true value
$\hat{}$ = estimated value
$\tilde{}$ = difference between true and estimated values

I. Introduction

THE new vision for space exploration will focus on sending humans to the moon and then to Mars. There are several challenges with manned Mars missions that did not exist in past robotic missions. One example is the need for precision landing so that a family of vehicles can be sent to the same location on the surface. Vehicles must land in close proximity to each other to provide the crew with easy access to all payloads. High landing accuracy will be required, and to achieve this level of accuracy, a controlled entry trajectory is critical. In addition, crewed missions will require not only hundreds of pounds of equipment, consumables, and experiments, but also additional living space for the astronauts during the many months they will be traveling to Mars. As a result, a larger and heavier vehicle is needed. The Mars ellipsled [1] described in this paper is one potential vehicle that meets these requirements.

One of the biggest challenges with the design of a guidance law or controller for a Mars vehicle is the uncertainty in the atmosphere characteristics. The Mars atmosphere has significant variations in density, as well as strong and sudden wind gusts that change greatly with seasons and with latitude and longitude [2,3]. In addition to the environmental uncertainties, the vehicle properties of a manned spacecraft are very likely to change during several months of travel. As a result, the controller must be able to compensate for any fluctuations in mass or vehicle properties, such as the changes in the center of gravity of the spacecraft.

Significant research has been performed to develop guidance and control algorithms for Mars entry. For example, [4,5] use neural networks in the guidance laws to compensate for the large uncertainties in the Martian atmosphere. Reference [6] describes the entry, descent, and landing phases for the Mars Exploration Rover missions. The vehicles were uncontrolled until a radar altimeter sensed the ground and then a solution was calculated to fire the retrorockets for the powered-descent phase. Reference [7] describes the use of a proportional–integral-–derivative controller to fire the retrorockets during the powered-descent phase.

Adaptive control has not been reported in the literature for the Mars entry problem, although it is an attractive solution, because it is capable of calculating and adjusting its own gain values while tracking a given reference trajectory. By having the gains adapt themselves with time, uncertainties in the atmosphere and vehicle properties are taken into account, providing robustness, and the controller is able to accurately track the reference command. This paper develops and evaluates an adaptive control system that is designed to handle significant environment and vehicle model uncertainties that are specific to the Mars entry problem. The unique contribution of this work is the development of an adaptive controller for Mars entry that provides good trajectory-tracking performance while in the presence of uncertainties in the atmospheric density, uncertainties in the vehicle aerodynamic coefficients, and uncertainties in the vehicle inertias. The plant used is the Mars ellipsled vehicle, and the scope of this work encompasses entry interface (labeled as EI in Fig. 1) until parachute deployment. Two different adaptive control algorithms are developed and evaluated: conventional model reference adaptive control (MRAC), which was previously developed by Narendra and Annaswamy [8], and the structured adaptive model inversion (SAMI) control algorithm [9], developed at Texas A&M University. The two candidate controllers are evaluated with numerical simulation to determine the severity of banking maneuvering that each can tolerate, in addition to test cases that determine the effect of errors in atmospheric density, vehicle aerodynamic coefficients, and vehicle inertias. The two controllers are also compared for trajectory-tracking performance during a complete simulated Mars entry scenario.

The paper is organized as follows. Section II presents a description of the Mars entry problem, including guidance and control of entry vehicles and modeling of the Mars atmosphere. A brief history of previous missions, as well as an overview of current research, is

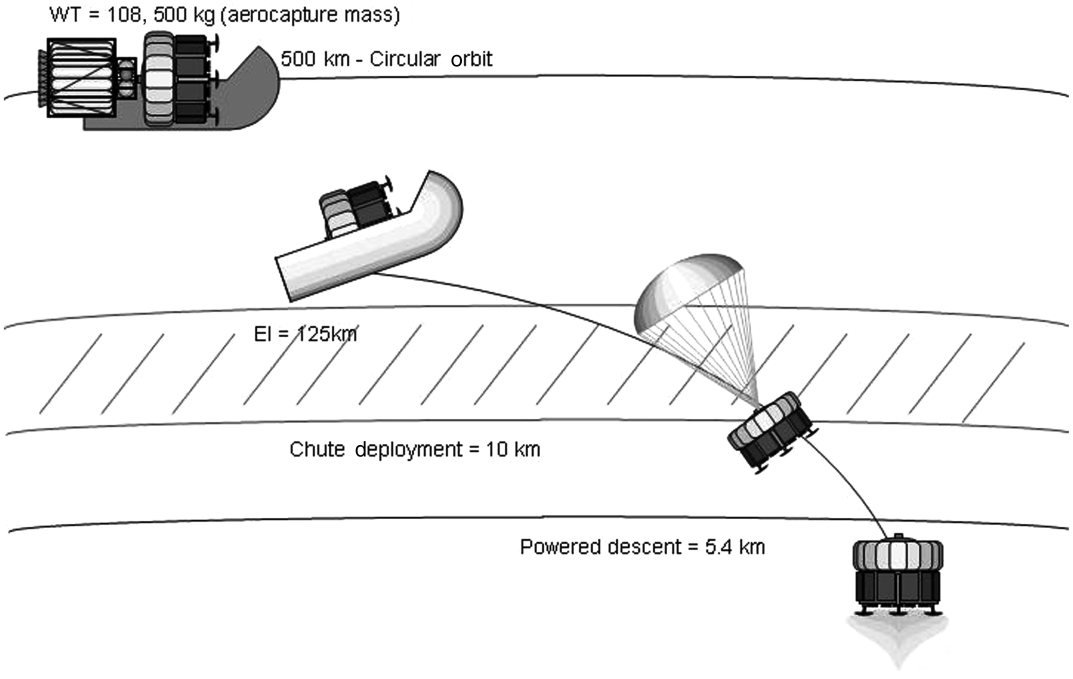

Fig. 1 Ellipsled entry trajectory [19].

included. A description of the Mars ellipsled vehicle is presented in Sec. III, followed by derivation of the equations of motion, modeling assumptions, and details of the numerical simulation in Sec. IV. Section V develops the MRAC and SAMI adaptive controllers, including implementation of both the system and control equations in the simulation. Finally, numerical simulation results are presented and discussed in Sec. VI, and conclusions are drawn in Sec. VII.

II. Mars Entry Problem

The Mars entry problem is challenging in many different ways. The variability in atmospheric characteristics of the planet presents challenges that do not exist when landing on Earth or on the moon. One of the more significant challenges when entering another planet's atmosphere is the position and velocity estimate errors from navigation at the entry interface. Initial errors are difficult to correct and may result in missing the target later. Therefore, the guidance system must be flexible to handle large initial errors.

The Martian atmosphere is dense enough to create significant heat rates and aerodynamic loads, which make it possible to skip out of the atmosphere. At the same time, it is not dense enough to slow the vehicle down as much as the Earth's atmosphere does. This has implications on the design of the trajectory, because the vehicle must slow down in time for safe parachute deployment and landing. Typically, a single parachute is used to slow down the vehicle, but for a heavy vehicle such as the ellipsled, the use of an additional supersonic parachute will be necessary. Another aspect to consider is the entry-interface velocity of the vehicle; higher velocities will present more difficulties in the design of the entry trajectory.

Currently, the most accurate model of the Martian atmosphere, the Mars Global Reference Atmosphere Model (Mars-GRAM) [10], is still not able to accurately predict the density and temperature variations or the strong and sudden wind gusts [11,12]. These properties also vary largely with seasons and latitude. All these factors present major challenges when designing guidance and control systems for Mars vehicles.

Another challenge that arises during Mars entry is the lack of translational controls on the vehicle. The only controls on a typical Mars lander vehicle are rotational, which means that the vehicle can maneuver solely by banking about the velocity vector following a series of roll reversals. Unlike a moon landing, where retrorockets are used to slow down the vehicle, a Mars lander can only use retrorockets during the terminal descent phase, when the dynamic pressure is sufficiently low enough.

As mentioned previously, the strict landing accuracy requirements are another challenge. Because a large landing ellipse with a footprint of approximately 100 km was acceptable for the Mars Pathfinder and Mars Exploration Rover robotic missions, an uncontrolled ballistic entry was used [6,13]. However, future manned missions will have landing requirements on the order of 5 km [14,15]. Therefore, having an active guidance system onboard the vehicle will be critical to meet landing accuracy requirements. Research is currently underway to investigate methods for meeting these strict landing requirements. Programs such as the Mars Science Laboratory and the Mars Surveyor are being used as prototype missions to design advanced guidance and control laws for Mars entry. Also, past knowledge with Earth reentry missions such as the Apollo and Mercury programs is being used as the basis for current Mars entry work by using Apollo-derived entry guidance algorithms [14,15].

A typical Mars entry vehicle consists of several parts: a lander containing a payload, an aeroshell that protects the lander from heating and aerodynamic forces during the atmospheric entry phase, and a parachute that helps decelerate the vehicle and separate it from the aeroshell. A typical Mars entry trajectory has the following phases:

1) In deorbit burn, the vehicle decelerates from its orbital velocity and reorients to its entry-interface attitude before entering the atmosphere. It maneuvers to the trim angle of attack and the correct initial flight-path angle.

2) In atmospheric entry, the vehicle flies through the atmosphere. The trajectory is calculated in real time by the guidance system.

3) In the parachute phase, the vehicle is decelerated aerodynamically with the parachute, and the lander is separated from its aeroshell.

4) In terminal descent, the vehicle detaches from the parachute and lands in a controlled manner. Retrorockets typically fire to further decelerate and reorient the lander to avoid any terrain hazards on the surface.

A. Entry Guidance and Control

The entry problem is generally divided in two parts: guidance design and control design. The guidance system calculates the entry trajectory in real time, in which the calculation is based upon heat load and aerodynamic load constraints. The control system then generates real-time attitude commands that will track the trajectory generated by the guidance system. Specifically, the aerodynamic forces are modulated to ensure satisfactory tracking of the reference trajectory that is being generated by an active guidance system.

1. Guidance

Trajectory generation for planetary entry is generally posed as an optimization problem in which the parachute deployment altitude is to be maximized. This allows additional flight time in the case in which the optimal conditions for the deployment of the parachute have not yet been reached. The optimization problem has path constraints on heat loads, gravity loads, and dynamic pressure. An active guidance routine calculates the flight-path angle γ needed to reach the final target. Current research on entry guidance algorithms for Mars missions are using Apollo command-capsule guidance, because this legacy algorithm is already man-rated. The Apollo guidance algorithm seeks to minimize errors in inertial position with respect to the landing target by following a reference trajectory chosen to satisfy aerodynamic or heat loads, but the reference trajectory itself is not precisely tracked. Direct control of the angle of attack is not available, and the aeroshell in these studies generates lift with a center-of-gravity offset and is designed to be trimmed during all phases of flight. To follow the trajectory generated by guidance, the magnitude of the lift and drag vectors are controlled by bank reversals, which is how the vehicle achieves the desired drag acceleration profile to meet its target. The vehicle is modeled as a point mass for the purpose of generating a trajectory, and the guidance equations typically assume that the vehicle flies at its trim condition. The only out-of-plane effect comes from the bank angle ϕ, which changes the lift component perpendicular to the velocity vector from L to $L\cos\phi$, thereby making the vehicle descend at a steeper or shallower flight-path angle.

Other vehicles that have similar guidance systems are the Mars Science Laboratory Mission [5] and the HL-20 [16], which is an Earth entry vehicle. The Mars Science Laboratory was actively controlled with reaction control-system (RCS) thrusters, and the HL-20 was controlled with aerodynamic surfaces. On the other hand, the Mars Exploration Rovers are an example of vehicles that did not require active attitude control. The aeroshell completely relies on aerodynamic and gyroscopic stability that minimize the angle-of-attack excursion [6].

2. Control

Ballistic entry vehicles have typically been designed with phase-plane controllers that simply roll the vehicle to the commanded bank angle. Much of the work is done by the guidance system, and the controller only needs to track the commanded bank angle. Most entry vehicles use RCS jets as their only control effectors. However, vehicles such as the Space Shuttle Orbiter, NASA's X-38, or HL-20 are designed to enter Earth's atmosphere using aerodynamic control surfaces in addition to RCS jets. Mars entry vehicles have rotational controls only, due to the added complexities of moving surfaces. The RCS jets are used to roll the vehicle about the velocity vector through several bank-angle reversals that are commanded by the guidance routine. By changing bank angle, the lift vector is rotated in the desired direction.

B. Mars Atmosphere

The observational data available for the Mars atmosphere are very sparse, compared with the data for the Earth's atmosphere. Models such as the Mars-GRAM [10] and the general circulation model database for Mars [17] are based on interpolation between the available observations and are subject to high uncertainties. Several researchers have attempted to model the Martian atmosphere. Empirical data are limited, and most efforts have focused on representing the variability of the atmospheric properties. For example, Duvall et al. [10] compare the data obtained by the Mars Global Surveyor with the Mars-GRAM atmospheric model to show that the model is accurate. However, density variations are still a concern for Mars mission designers. Figure 2 is a good representation of how the density for a given altitude can vary greatly with solar longitude L_s. Another example of density variations in the Mars atmosphere is presented in [18]. The Mars-GRAM model was used for the design of the Mars Pathfinder Mission, and density variations were taken into account. Figure 3 is a graphic representation of the density variations for different atmospheric models. In addition to atmospheric parameter variations, winds are an important issue to consider when designing a guidance system. For example, the recent Mars Exploration Rover missions used [10] for wind variations during entry at both sites. The work presented here uses the Mars-GRAM both in the simulations and as a basis to compare the results for cases with atmospheric density uncertainties.

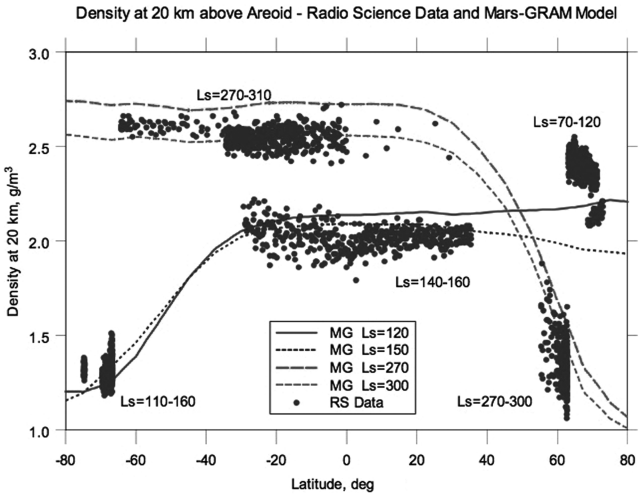

Fig. 2 Comparison of density at 20-km altitude from Mars Global Surveyor radio science observations and Mars-GRAM 2001 [10].

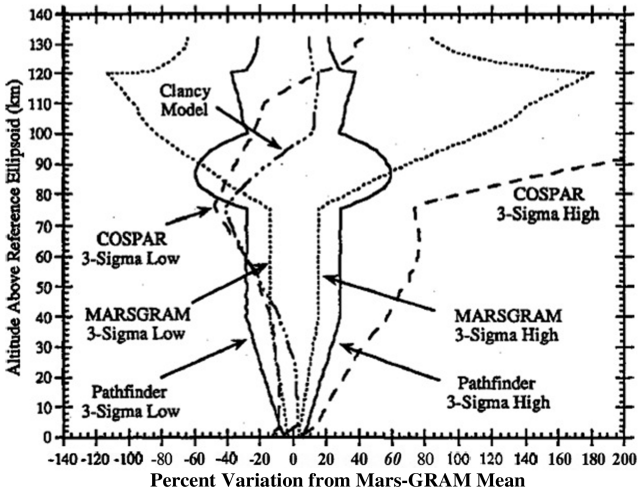

Fig. 3 Mars atmospheric density models compared with the Mars-GRAM mean [18].

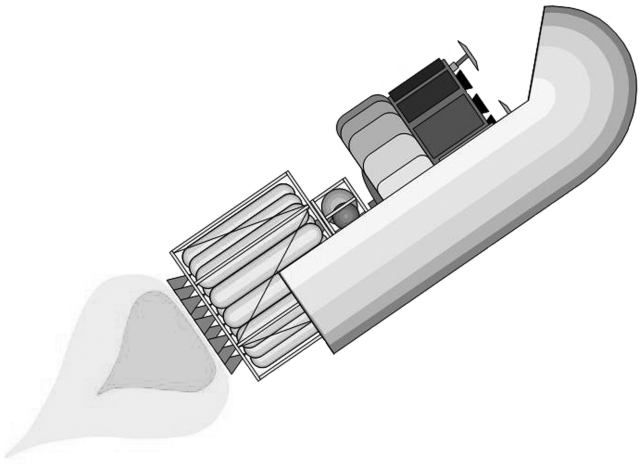

Fig. 4 Mars ellipsled [19].

III. Mars Ellipsled Entry Vehicle

Future manned missions to Mars will require much larger and heavier vehicles than those used in the past. The missions will last several months, and these vehicles must be able to provide life support for the crew, as well as to carry large quantities of consumables and scientific equipment. Thus, the conical shapes used previously for robotic missions or relatively short lunar manned missions will not suffice. If the same conical-shaped vehicle were scaled up, it would be so large in diameter that it might not fit on a practical-sized launch vehicle. The ellipsled is an alternate shape for an aeroshell that could carry several metric tons stacked along the length of the vehicle, yet could fit in an existing launch vehicle. The ellipsled can carry up to six crew members to Mars, weighs up to 78 t, and has a length of approximately 20 m (Fig. 4). One of the main advantages of using an aeroshell with this shape is that it was designed to be one-half of the launch vehicle shroud on Earth, thereby not incurring additional weight cost for the entry-vehicle shell. Another advantage of this shape is a lift-to-drag value of approximately 0.46. This value has historically been around 0.3 for conical shapes such as the Apollo entry capsules. A previous study performed at the NASA Johnson Space Center [19] concluded that the ellipsled has enough stability and flight mechanics margins to take humans to Mars [1].

A scaled-down model of the ellipsled was used for the present work. The vehicle was modeled as a cylinder with a diameter of 3.75 m, a length of 6.323 m, and a mass of 3000 kg. The center of gravity in the x direction, x_{cg}, and in the z direction, z_{cg}, are offset for maneuverability. Tables 1 and 2 list the mass and geometric properties of the ellipsled.

The ellipsled used previously has 18 reaction control-system jets located in the aft part of the vehicle. There are nine jets on each side, located in three clusters of three jets each: three side jets, three up jets, and three down jets. The three side jets on each side of the vehicle are

Table 1 Ellipsled mass and inertia properties

Mass	3000 kg
I_{xx}	2983 kg · m^2
I_{yy}	4909 kg · m^2
I_{zz}	5683 kg · m^2

Table 2 Ellipsled geometric properties

Reference area	S	11.045 m^2
length	l	6.323 m
x center of gravity	x_{cg}	0.182 m
y center of gravity	y_{cg}	0 m
z center of gravity	z_{cg}	−0.175 m

Table 3 Reaction control-system jet properties

	Single jet thrust, N	Moment arm, m	Minimum torque, N · m	Maximum torque, N · m
Roll	28	1.88	2 jets: 105	6 jets: 316
Pitch	28	2.98	2 jets: 83	6 jets: 501
Yaw	95	2.98	1 jet: 283	3 jets: 849

used only for yaw control. The three up jets and three down jets on each side of the vehicle are capable of both pitch and roll control. The maximum pitch torque is produced by firing six jets: three up jets on each side for a nose-down maneuver or three down jets on each side for a nose-up maneuver. The maximum roll torque is produced by firing six jets: three up on one side and three down on the opposite side of the vehicle. The maximum yaw torque is produced by firing a maximum of three side jets on either side of the vehicle. Table 3 provides characteristics of the thrust, moment arm, and minimum and maximum torques that can be generated. It is important to note that these values are used here as guidelines rather than strict limits for the design of the adaptive controller. This is because the control input is calculated as a continuous signal, and this signal would have to be converted into discrete jet firings.

The RCS jets are designed to provide angular accelerations of at least 5 deg/s^2. They can be used to keep the angle of attack at its trim value and to roll the vehicle about the velocity vector to track a bank-angle profile. Here, it is assumed that the moment arms of the RCS jets are constant with respect to the center of gravity of the vehicle. Additionally, it is assumed that there is no change in mass or inertia properties due to fuel consumption. The aerodynamic data were obtained from [19] and are presented in Table 4.

An example mission would take two ellipsleds to Mars. One would carry an astronaut habitat and the other would carry the crew and life support equipment. Both vehicles need to land at approximately the same location on the Mars surface.

IV. Entry Simulation

This section describes the entry simulation used to evaluate the two adaptive control systems and includes a detailed development of the translational and rotational equations of motion for the ellipsled. The simulation is nonlinear and its five degrees of freedom include the altitude above the surface of the planet, the downrange distance, and the three rotational degrees of freedom. The ellipsled is modeled as a rigid cylinder with a symmetric inertia matrix. Like many entry vehicles, the ellipsled is designed to have both aerodynamic stability (statically stable in pitch) and gyroscopic stability so that only minimal RCS jet inputs are needed to modulate the angle of attack at its trim value during entry. We apply the standard entry-vehicle assumption that the minimal RCS pitch control is negligible and can be decoupled from the bank-angle control. The assumption is implemented by setting the vehicle to be open loop in pitch, with the angle of attack remaining at or very near the trim value during entry because of the static stability property. Reference [19] concludes that the trim angle of attack for the ellipsled is 55 deg and that the center of gravity of the cylinder is shifted from the center of the cylinder in the x and z directions by the following amounts:

$$x_{\text{cg}} = 0.182 \text{ m} \tag{1}$$

$$z_{\text{cg}} = -0.175 \text{ m} \tag{2}$$

Table 4 Ellipsled aerodynamics

α, deg	C_L	C_D	C_{n_β}	$C_{m\alpha}$	C_{l_β}
45	0.652	1.568	−0.02	0.037	−2.279
50	0.659	1.740	0	0.019	−2.354
55	0.633	1.910	0.015	0.000	−2.414
60	0.573	2.069	0.034	−0.211	−2.462
65	0.481	2.208	0.05	−0.428	−2.495

To validate the aerodynamic and gyroscopic stability assumptions, a nonlinear, three-degree-of-freedom, open-loop simulation was used to evaluate three different trim angles of attack. Figure 5 shows that for an ellipsled that is statically stable in pitch, it remains trimmed in pitch for an initial value of $\alpha = 55$ deg. This result validates the assumption that the angle of attack remains constant during entry, and so the minimal RCS pitch control jets can be considered to be negligible. For the evaluations conducted here, the angle of attack remains constant at 55 deg and the controller tracks a bank-angle command.

The entry problem is typically divided into two parts: guidance or trajectory generation and control design. The translational equations of motion are part of the guidance system, and the rotational equations of motion are part of the control system. The translational and rotational equations for the ellipsled during its entry phase are developed next.

A. Translational Equations of Motion

The translational kinematics for the mass center of the vehicle are given in an inertial planet-fixed frame, as shown in Fig. 6. This figure shows the velocity vector at the mass center, which is related to the inertial reference frame $\{\mathbf{i}\}$ through two angles: the heading angle ξ

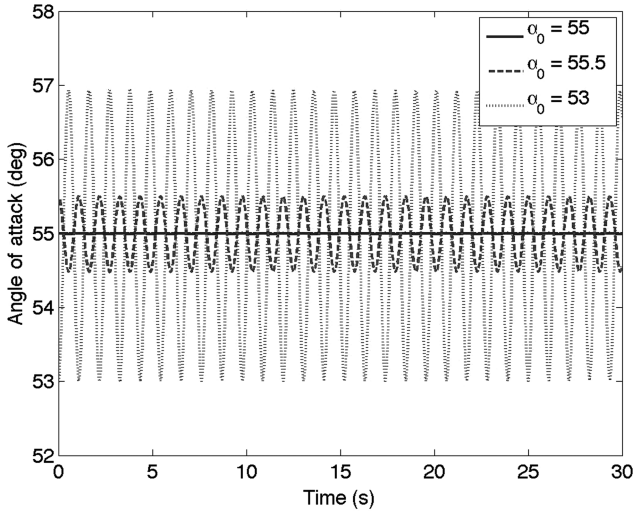

Fig. 5 Ellipsled trim angle of attack.

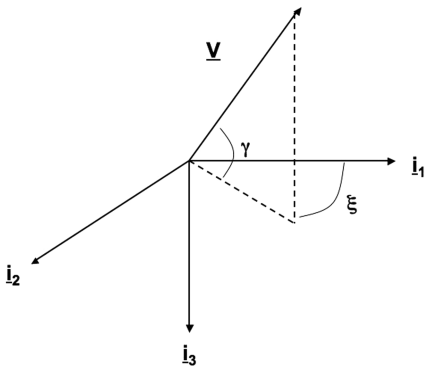

Fig. 6 Inertial reference frame.

and the flight-path angle γ. The velocity vector $\mathbf{v}$ can be expressed in Cartesian coordinates:

$$\mathbf{v} = \dot{x}\hat{\mathbf{i}}_1 + \dot{y}\hat{\mathbf{i}}_2 + \dot{z}\hat{\mathbf{i}}_3 \tag{3}$$

where $\dot{z} = -\dot{h}$, and h is the altitude. This vector can also be expressed in a different set of coordinates as a function of its magnitude $v = |\mathbf{v}|$ and the angles ξ and γ:

$$\mathbf{v} = v\cos\gamma\cos\xi\hat{\mathbf{i}}_1 + v\cos\gamma\sin\xi\hat{\mathbf{i}}_2 - v\sin\gamma\hat{\mathbf{i}}_3 \tag{4}$$

By setting both equations equal to each other, it is possible to obtain equations for one set of coordinates in terms of the other set of coordinates, as follows:

$$\dot{x} = v\cos\gamma\cos\xi \tag{5}$$

$$\dot{y} = v\cos\gamma\sin\xi \tag{6}$$

$$\dot{h} = -v\sin\gamma \tag{7}$$

where x is the downrange distance, y is the crossrange distance, and h is the altitude above the surface of Mars. Here, the heading angle is assumed to be zero, due to the lack of an active guidance scheme.

The preceding translational equations of motion are written in the inertial frame. However, it is also necessary to write them in a body-fixed frame with the origin at the mass center of the vehicle. The direction cosine matrix to transfer from the inertial frame $\{\mathbf{i}\}$ to the body-fixed frame $\{\mathbf{b}\}$ is calculated using a 3-2-1 Euler angle sequence through the yaw angle Ψ, the pitch angle Θ, and the roll angle Φ. This rotation matrix is given by

$$[\mathbf{n}]_b = [C_1(\Phi)][C_2(\Theta)][C_3(\Psi)][\mathbf{n}]_i \tag{8}$$

The translational equations for the center of mass can now be written in the body frame as a function of the magnitude of the velocity vector and the aerodynamic angles α and β, as shown in Eq. (9). Figure 7 is a graphic representation of this.

$$[\mathbf{v}]_b = \begin{bmatrix} v\cos\beta\cos\alpha \\ v\sin\beta\cos\alpha \\ v\sin\alpha \end{bmatrix} \tag{9}$$

Having developed the translational kinematics in the body frame, the dynamics are now derived. The external forces acting on a ballistic entry vehicle are the aerodynamic forces and the gravity force. These forces are typically expressed in a reference frame called the wind frame $\{\mathbf{w}\}$. To obtain the forces for the translational equations with the vehicle coordinatized in the wind frame, it is necessary to describe the relationship between the body frame, inertial frame, and wind frame. To transfer from the inertial frame to the wind frame, another 3-2-1 Euler angle sequence is used. In this transformation, the frame is rotated through the heading angle ξ, flight-path angle γ, and bank angle ϕ. A graphic representation of this is given in Fig. 8.

In general, the coordinatization of any vector in the wind frame is given by

$$[\mathbf{n}]_w = [C_1(\phi)][C_2(\gamma)][C_3(\xi)][\mathbf{n}]_i \tag{10}$$

Now the dynamic equations for the vehicle can be written in the wind frame. Consider the special case in which the heading angle $\xi = 0$. First, the kinematics for the mass center are developed; subsequently, the forces acting on the vehicle are described with a free-body diagram. The translational kinematics for the center of mass are given by

$$\mathbf{v} = v\hat{\mathbf{w}}_1 \tag{11}$$

$$\mathbf{a} = \frac{{}^w\mathrm{d}}{\mathrm{d}t}(\mathbf{v}) + \omega_{w/i} \times \mathbf{v} \tag{12}$$

where

$$[\omega_{w/i}]_w = \begin{bmatrix} -\dot{\xi}\sin\gamma + \dot{\phi} \\ \dot{\xi}\cos\gamma\sin\phi + \dot{\gamma}\cos\phi \\ \dot{\xi}\cos\gamma\cos\phi + \dot{\gamma}\sin\phi \end{bmatrix} \tag{13}$$

Substituting $[\omega_{w/i}]_w$ into the acceleration equation results in

$$\mathbf{a} = \dot{v}\hat{\mathbf{w}}_1 - v\dot{\gamma}\sin\phi\hat{\mathbf{w}}_2 - v\dot{\gamma}\cos\phi\hat{\mathbf{w}}_3 \tag{14}$$

There are three external forces acting on the ellipsled, as shown in Fig. 9: lift, drag, and gravity. The lift vector $\mathbf{L}$ is perpendicular to the velocity vector, the drag vector $\mathbf{D}$ is in the direction opposite to the velocity vector, and the gravity vector $\mathbf{g}$ points in the positive z axis of the planet-fixed reference frame. The forces in newtons are calculated in Eqs. (15–17):

$$\mathbf{L} = -\bar{q}Sc_{L_\alpha}\alpha\hat{\mathbf{w}}_3 \tag{15}$$

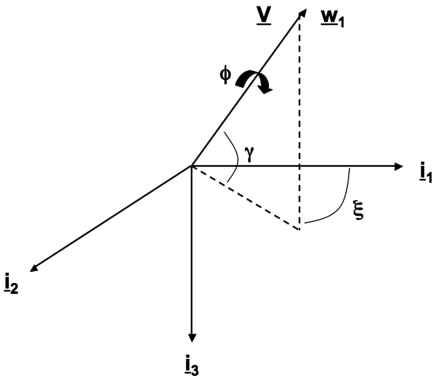

Fig. 8 Wind reference frame.

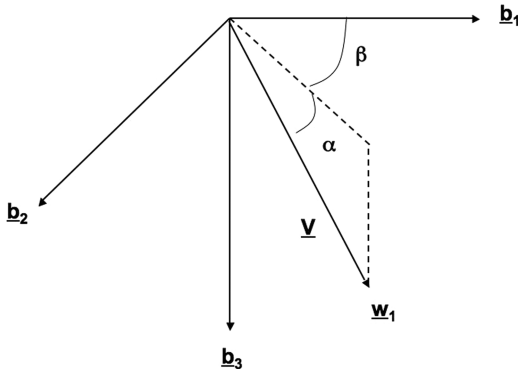

Fig. 7 Body-fixed reference frame.

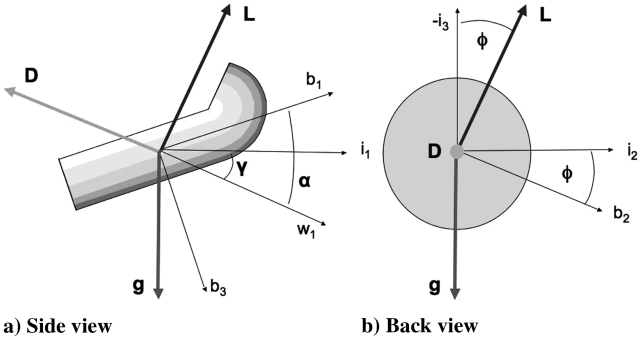

a) Side view **b) Back view**

Fig. 9 Ellipsled free-body diagram.

$$\mathbf{D} = -\bar{q}Sc_{D_\alpha}\alpha\hat{\mathbf{w}}_\mathbf{1} \tag{16}$$

$$\mathbf{g} = mg\hat{\mathbf{i}}_\mathbf{3} \tag{17}$$

The total force vector **F** can now be written as follows:

$$[\mathbf{F}]_w = \begin{bmatrix} -D - mg\sin\gamma \\ mg\cos\gamma\sin\phi \\ -L + mg\cos\gamma\cos\phi \end{bmatrix} \tag{18}$$

From Newton's second law, the dynamic translational equations of the mass center of the vehicle are given by

$$[\mathbf{F}]_w = m[\mathbf{a}]_w \tag{19}$$

$$-D - mg\sin\gamma = m\dot{v} \tag{20}$$

$$mg\cos\gamma\sin\phi = -mv\dot{\gamma}\sin\phi \tag{21}$$

$$-L + mg\cos\gamma\cos\phi = -mv\dot{\gamma}\cos\phi \tag{22}$$

Rearranging the first equation and adding the second and third equations results in

$$\dot{v} = -\frac{D}{m} - g\sin\gamma \tag{23}$$

$$\dot{\gamma} = \frac{L}{mv}\cos\phi - \frac{g}{v}\cos\gamma \tag{24}$$

These equations are the translational equations of motion or guidance equations for the ellipsled.

B. Rotational Equations of Motion

This section develops the rotational equations of motion for the vehicle about its mass center. The rotational kinematic equations for the ellipsled can be expressed in the body frame as

$$\begin{bmatrix} \dot{\Psi} \\ \dot{\Theta} \\ \dot{\Phi} \end{bmatrix} = [A_{321}(\ \Psi \quad \Theta \quad \Phi\ )][\omega]_b \tag{25}$$

where A_{321} is the direction cosine matrix to transform from the inertial frame to the body frame. The angular velocity of the vehicle in the body-fixed frame can also be written as

$$[\mathbf{w}_{b/i}]_b = [\mathbf{w}_{b/w}]_b + [\mathbf{w}_{w/i}]_b \tag{26}$$

or using the direction cosine matrix to transform from the wind frame to the body frame,

$$[\mathbf{w}_{b/i}]_b = [C_w^b]([\mathbf{w}_{b/w}]_w + [\mathbf{w}_{w/i}]_w) \tag{27}$$

The matrix $[C_w^b]$ is given in terms of the aerodynamic angles α and β from Fig. 7,

$$[C_w^b] = [C_2(\alpha)][C_3(-\beta)] = \begin{bmatrix} \cos\alpha\cos\beta & -\cos\alpha\sin\beta & -\sin\alpha \\ \sin\beta & \cos\beta & 0 \\ \sin\alpha\cos\beta & -\sin\alpha\sin\beta & \cos\alpha \end{bmatrix} \tag{28}$$

and the body angular velocity is

$$\omega_{b/w} = \dot{\alpha}\hat{\mathbf{b}}_\mathbf{2} - \dot{\beta}\hat{\mathbf{w}}_\mathbf{3} \tag{29}$$

However, it was assumed that the angle of attack α is held constant throughout the entry portion of the simulation. Therefore, the angular velocity coordinatized in the wind frame can be written as

$$[\omega_{b/w}]_w = [\,0 \quad 0 \quad -\dot{\beta}\,]^T \tag{30}$$

Substituting Eqs. (14), (28), and (30), into Eq. (26), the rotational kinematic equations for the ellipsled are obtained:

$$\begin{bmatrix} p \\ q \\ r \end{bmatrix} = \begin{bmatrix} \cos\alpha\cos\beta & -\cos\alpha\sin\beta & -\sin\alpha \\ \sin\beta & \cos\beta & 0 \\ \sin\alpha\cos\beta & -\sin\alpha\sin\beta & \cos\alpha \end{bmatrix} \begin{bmatrix} \dot{\phi} \\ \dot{\gamma}\cos\phi \\ -\dot{\beta} - \dot{\gamma}\sin\phi \end{bmatrix} \tag{31}$$

Rearranging,

$$\begin{bmatrix} p \\ q \\ r \end{bmatrix} = \begin{bmatrix} \cos\alpha\cos\beta & -\cos\alpha\sin\beta\cos\phi + \sin\alpha\sin\phi & \sin\alpha \\ \sin\beta & \cos\beta\cos\phi & 0 \\ \sin\alpha\cos\beta & -\sin\alpha\sin\beta\sin\phi - \cos\alpha\sin\phi & -\cos\alpha \end{bmatrix} \begin{bmatrix} \dot{\phi} \\ \dot{\gamma} \\ \dot{\beta} \end{bmatrix} \tag{32}$$

Taking the inverse of Eq. (32) provides the kinematic equation for the ellipsled:

$$\begin{bmatrix} \dot{\phi} \\ \dot{\gamma} \\ \dot{\beta} \end{bmatrix} = \begin{bmatrix} \cos\alpha\cos\beta & \sin\beta & \sin\alpha\cos\beta \\ -\sin\alpha\cos\beta/\cos\phi & \cos\beta/\cos\phi & -\sin\alpha\sin\beta/\cos\phi \\ \cos\alpha\sin\beta\tan\phi + \sin\alpha & -\cos\beta\tan\phi & \sin\alpha\sin\beta\tan\phi - \cos\alpha \end{bmatrix} \begin{bmatrix} p \\ q \\ r \end{bmatrix} \tag{33}$$

Note that Eq. (33) is not a conventional kinematic matrix because the reference trajectory is given in the wind frame. By evaluating the determinant of this matrix, it was determined that it becomes singular for combinations of angle of attack, sideslip angle, and bank angle, which make the following expression equal to zero:

$$\tfrac{1}{4}(2\cos\beta\tan\phi + \cos 2\alpha - \cos 2\beta - \cos(2\alpha - 2\beta) - 2\tan\phi\cos(-\beta + 2\alpha) - 3)/\cos\phi \tag{34}$$

The ellipsled is assumed to be a rigid body, and so Euler's rotational equations are used:

$$[I]\dot{\omega} + \omega \times [I]\omega = \mathbf{f} \tag{35}$$

where **f** is the sum of the aerodynamic moments $\mathcal{L}$, $\mathcal{M}$, and $\mathcal{N}$, and the control input **u** is from the reaction control-system jets. The magnitudes of the aerodynamic moments are

$$\mathcal{L} = \bar{q}S_{\text{ref}}l_{\text{ref}}c_{l_\beta}\beta \tag{36}$$

$$\mathcal{M} = \bar{q}S_{\text{ref}}l_{\text{ref}}c_{m_\alpha}\alpha \tag{37}$$

$$\mathcal{N} = \bar{q} S_{\text{ref}} l_{\text{ref}} c_{n_\beta} \beta \tag{38}$$

The magnitude of the control input **u** is given by thrust times the moment arm for each jet. Controller synthesis is described in detail in a later section.

There are several papers in the literature that discuss optimal guidance and use similar point-mass translational equations plus the bank-angle equation to calculate the necessary entry trajectory in terms of bank-angle commands. Some examples of problems that use these equations can be found in [4,15,16]. In all of these examples, as well as for the ellipsled, the only two states that are controlled are the angle of attack (which is regulated to its trim value) and the bank angle (which is used to track the necessary roll reversals commanded by guidance).

V. Adaptive Control

Designing a controller for a physical system presents several challenges. Typically, the optimum balance between model fidelity and simplicity of the mathematical model of a system is difficult to achieve. In addition, there are usually unexpected errors or variations in the model of a system and in the model of the environment in which it operates. The main goal of a control system is thus to maintain correct system operation in the presence of all modeling errors and changes in operating conditions. For systems that have known bounds on the uncertainties, it is possible to design a controller that can be tuned a priori to compensate for these errors. Gain scheduling [20] and robust control [21] are two such methods for this. The space shuttle is an example of an entry vehicle that uses gain scheduling during the entry phase [22]. The scheduling is based on dynamic pressure and Mach number. However, these methodologies work well for Earth entry because it is possible to obtain highly accurate atmospheric data. In cases in which the system uncertainties are large and highly unpredictable, such as the atmospheric density and wind gusts in the Martian atmosphere, a controller with continuous adaptation to achieve and maintain acceptable performance is beneficial.

Adaptive control is a class of controllers that are particularly suitable for systems that have uncertain parameters before and during their operation. A common characteristic of adaptive controllers is the ability to tune gains in real time through a learning mechanism based on current performance. There are two main classes of adaptive control: MRAC and self-tuning control [23]. The main difference between these two methods is that a MRAC controller directly calculates the control law based on measured signals, whereas a self-tuning controller estimates the plant parameters based on the reference plant parameters and calculates the control law indirectly based on these estimates. For this work, two controllers are designed and implemented. The first controller is based on the standard MRAC model found in the literature [8,20,23,24]. The second controller is based on the SAMI [9] methodology developed at Texas A&M University. The most important difference between the two methodologies is that the MRAC controller adapts the controller gains to achieve tracking error convergence, whereas the SAMI controller can adapt specifically for the lack of knowledge in the vehicle properties or Mars atmospheric properties.

A. Model Reference Adaptive Control

The goal of a MRAC system is to track the output of a reference model by enforcing error convergence. This is done by continuously calculating the controller gains through an adaptation mechanism. A block diagram of a typical MRAC system [23] is presented in Fig. 10. The reference model is used to generate an ideal output y_m to be followed by the plant output y. The control input u is calculated based on the adaptation laws that depend on e, the error between the reference and actual model outputs. However, it is not always necessary to have an ideal model to generate a reference trajectory. It is possible to use a precomputed trajectory, which must meet certain conditions. For example, in the case of the Mars ellipsled, the reference trajectory would come from an active guidance routine. For the MRAC problem, the plant model contains several uncertain parameters but has a known structure. The scalar system derivation here can be extended to vector functions without loss of generality. The differential equation for the system or the reference model can be either linear or nonlinear; in general, it has the form

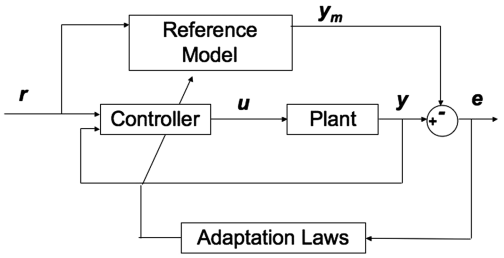

Fig. 10 MRAC block diagram [23].

$$\dot{x} = f(x) + u \tag{39}$$

The controller takes the error dynamics as an input to adjust its own gains with time. The error is the difference between the current output of the system and the reference trajectory. The control objective is to minimize the error between the outputs, and so perfect tracking of the states is not always achieved. The adaptation mechanism for the control law can vary from one case to another, depending on the form of the dynamic equations of the system. In general, it is possible to find a differential equation for each of the gains in the control law. With time, these gains will learn the ideal value needed to achieve convergence of the error. The control law u has the form

$$u = \tilde{a}_r r + \tilde{a}_\omega \omega \tag{40}$$

where ω and r are the angular velocity and the reference angular velocity, respectively, and $\tilde{a}_r$ and $\tilde{a}_w$ are the adaptive gains that change with time. Lyapunov stability theory is used to obtain the differential equations for these gains to ensure stable error dynamics [8,20,23]. In this case, the Lyapunov function from Eq. (41) and its derivative shown in Eq. (42) are used to derive the adaptation equations for $\tilde{a}_r$ and $\tilde{a}_\omega$, as follows:

$$V(e, \tilde{a}_r, \tilde{a}_\omega) = \frac{1}{2} e^2 + \frac{1}{2\Gamma} |b_p| (\tilde{a}_r^2 + \tilde{a}_w^2) \tag{41}$$

$$\dot{V}(e, \dot{e}, \tilde{a}_r, \dot{\tilde{a}}_r, \tilde{a}_\omega, \dot{\tilde{a}}_\omega) = e\dot{e} + \frac{1}{\Gamma} |b_p| (\tilde{a}_r \dot{\tilde{a}}_r + \tilde{a}_\omega \dot{\tilde{a}}_\omega) \tag{42}$$

where $e = \omega - \omega_r$, and the subscript r denotes the reference. The error dynamics are substituted into the derivative of the Lyapunov function such that

$$\dot{e} = \dot{\omega} - \dot{\omega}_r \tag{43}$$

where

$$\dot{\omega} = f(\omega, I) + b_p u \tag{44}$$

$$\dot{\omega}_r = a_m \omega_r + b_m r \tag{45}$$

Combining the preceding equations results in

$$\dot{e} = f(\omega, I) + b_p u + a_m \omega_r + b_m r = f(\omega, I) + b_p (\hat{a}_r r + \hat{a}_\omega \omega) + a_m \omega_r + b_m r \tag{46}$$

where $\hat{a}_r$ and $\hat{a}_\omega$ are the parameter estimates. By setting Eq. (46), the derivative of the error, equal to zero and equating coefficients, the ideal values of the gains a_ω^* and a_r^* can be solved for:

$$f(\omega, I) + b_p (\hat{a}_r \omega_{\text{ref}} + \hat{a}_w \omega) = -a_m \omega_r - b_m r \tag{47}$$

$$a_\omega^* = -\frac{a_m}{b_p} - \frac{f(\omega, I)}{b_p \omega} \tag{48}$$

$$a_r^* = \frac{b_m}{b_p} \tag{49}$$

Clearly, the ideal values cannot be calculated because the true values for the plant parameters are unknown. This can be overcome by deriving adaptive laws for the error between the estimates and the true values instead of adaptive laws for the estimates directly. The following equations show the derivative of the error in terms of the true parameters and their estimates. These results are substituted into the Lyapunov function in subsequent steps to finally obtain the adaptation laws for the controller gains:

$$\begin{aligned}
\dot{e} &= -a_m(\omega - \omega_r) + (a_m + b_p\hat{a}_\omega)\omega + f(\omega, I) \\
&\quad + b_p(-b_m + \hat{a}_r b_p)r = -a_m e + (a_m + b_p\hat{a}_\omega)\omega \\
&\quad + f(\omega, I) + b_p\left(-\frac{b_m}{b_p} + \hat{a}_r\right)r = -a_m e \\
&\quad + \left(\frac{b_p a_m}{b_p} + b_p\hat{a}_\omega + \frac{f(\omega, I)b_p}{\omega b_p}\right)\omega + b_p\left(-\frac{b_m}{b_p} + \hat{a}_r\right)r \\
&= -a_m e + b_p\left(\frac{a_m}{b_p} + \frac{f(\omega, I)}{\omega b_p} + \hat{a}_\omega\right)\omega + b_p(\hat{a}_r - a_r^*)r \\
&= -a_m e + b_p(\hat{a}_\omega - a_\omega^*)\omega + b_p(\hat{a}_r - a_r^*)r
\end{aligned} \tag{50}$$

where $\hat{a}_\omega$ and $\hat{a}_r$ are the estimated gains, and a_ω^* and a_r^* are the ideal values of the gains. As mentioned earlier, it is desired to derive adaptive laws for the difference of the true parameters and their estimates. These new parameters are defined as

$$\tilde{a}_\omega = \hat{a}_\omega - a_\omega^* \tag{51}$$

$$\tilde{a}_r = \hat{a}_r - a_r^* \tag{52}$$

and the equation that describes the error dynamics becomes

$$\dot{e} = -a_m e + b_p(\tilde{a}_\omega \omega + \tilde{a}_r r) \tag{53}$$

Substituting Eq. (53) into the expression for $\dot{V}$ in Eq. (42) produces

$$\dot{V} = -a_m e^2 + b_p\left[\left(e\omega + \frac{1}{\gamma}\dot{\tilde{a}}_w\right)\tilde{a}_w + \left(er + \frac{1}{\gamma}\dot{\tilde{a}}_r\right)\tilde{a}_r\right] \tag{54}$$

Now the adaptive laws can be found by setting the second and third terms of $\dot{V}$ equal to zero. The resulting equations dictate the adaptation mechanism for $\tilde{a}_r$ and $\tilde{a}_w$. These gains are proportional to a constant parameter Γ called the learning rate, which determines how fast the adaptation occurs, as shown in Eqs. (55) and (56):

$$\dot{\tilde{a}}_r = -\Gamma e \omega_{\text{ref}} \tag{55}$$

$$\dot{\tilde{a}}_w = -\Gamma e \omega \tag{56}$$

Selection of values for the learning rate Γ and initial values for the gains are tuning parameters for the controller, which will be discussed in Sec. VI.

Because the error dynamics in Eq. (53) have time-dependent terms on the right-hand side, the system is nonautonomous, and Barbalat's lemma [23] is used to analyze stability. With the choice of Lyapunov function in Eq. (54), $\dot{V} \leq 0$. Because $\dot{V} \leq 0$ and $V > 0$, all terms in $V \in \mathcal{L}_\infty$ (i.e., $\{e, \dot{e}, \tilde{a}_r, \tilde{a}_w\} \in \mathcal{L}_\infty$). Integrating $\dot{V}$ over $[0, \infty]$, it can be shown that $e \in \mathcal{L}_2$ as well. Thus, $e \in \mathcal{L}_2 \cap \mathcal{L}_\infty$. Now consider $\dot{e}$ in Eq. (53). All terms on the right-hand side are bounded: r is bounded by choice, w is bounded because e is bounded, and w_r is bounded; thus, $\dot{e} \in \mathcal{L}_\infty$. Now, because $\mathcal{L}_2 \in \mathcal{L}_\infty$ and $\dot{e} \in \mathcal{L}_\infty$, Barbalat's lemma states that $e \to 0$ as $t \to \infty$, and hence the states of the plant converge asymptotically to the reference states.

B. Structured Adaptive Model Inversion Control

The second adaptive control approach used here, SAMI [9,25,26], is based on the concepts of structured model reference adaptive control [27] as well as feedback linearization and dynamic inversion [23]. For dynamic inversion to work properly, it is necessary to have an accurate mathematical model of the plant so that the dynamics can be cancelled out exactly. Because this is not possible due to the inherent uncertainties in physical systems, an adaptive controller is wrapped around the dynamic inversion controller to compensate for these errors. The concept of structured model reference adaptive control takes advantage of the fact that equations of motion of a system can be separated into distinct dynamic and kinematic parts. The kinematic equations are exactly known, and so all of the uncertainty is contained in the dynamic equations. Therefore, the adaptation mechanism for the system is restricted only to the momentum-level equations that contain the uncertain parameters such as mass and inertia [27].

SAMI has been applied to trajectory tracking with smooth maneuvers and can handle large model errors [28] and bounded disturbances. Specifically, it has been used for tracking of aggressive aircraft maneuvers [29] and spacecraft maneuvers with control-moment gyros [25]. However, because SAMI must track a singularity-free trajectory, there can be no unmodeled dynamics. Because of the control effector configuration of the Mars ellipsled, one of the challenges of the present work is to use a SAMI controller to track nonsmooth discrete commands in the form of a series of step inputs. There is a singularity each time a new command is given, and so a smooth polynomial curve is fitted to the reference so that the controller can track it. Even with a smoothed trajectory, consideration must be given to the slopes of the commands being steep, possibly leading to large control inputs.

The development of the SAMI equations for this paper follows the work of Junkins et al. [29]. The dynamic and kinematic equations have the form of Eqs. (57) and (58):

$$\dot{q} = f(q, \omega) \tag{57}$$

$$\dot{\omega} = g(q, \omega, p) + h(q, \omega, p)u + H(q, \omega) \tag{58}$$

where q is the attitude vector expressed in terms of the classical Rodrigues parameters [30] and ω is the angular velocity vector. The terms $f(q, \omega, p)$, $g(q, \omega, p)$, $h(q, \omega, p)$, and $H(q, \omega, p)$ are continuous functions, and p is a vector of uncertain parameters. For the Mars ellipsled, Eq. (57) is the kinematic equation for rigid-body motion, and Eq. (58) can be represented by Euler's rotational equations of motion, as shown next:

$$\dot{q} = A(q)\omega \tag{59}$$

$$I^*\dot{\omega} = -\omega \times I^*\omega + u \tag{60}$$

where $A(q)$ is the kinematic matrix in terms of classical Rodrigues parameters, I^* is the true inertia matrix of the vehicle, and u is the control input. Because controller seeks to drive the tracking error to zero, the error dynamics are prescribed as

$$\ddot{e} + C\dot{e} + Ke = 0 \tag{61}$$

where C and K are positive-definite matrices chosen by the designer, and the error is defined as $e = q - q_r$. To obtain the first and second derivatives of the error, the kinematic equation is differentiated with respect to time and the dynamic equation is substituted into the expression as follows:

$$\begin{aligned}
\ddot{q} &= \frac{\partial f}{\partial q}\dot{q} + \frac{\partial f}{\partial \omega}\dot{\omega} = \frac{\partial f}{\partial q}\dot{q} + \frac{\partial f}{\partial \omega}[g(q, \omega, p) + h(\sigma, \omega, p)u \\
&\quad + H(q, \omega)]
\end{aligned} \tag{62}$$

Now that expressions for q, $\dot{q}$, and $\ddot{q}$ are available, with q_r, $\dot{q}_r$, and $\ddot{q}_r$ prescribed, they can be substituted into the error dynamics equation to obtain

$$\frac{\partial f}{\partial q}\dot{q} + \frac{\partial f}{\partial \omega}[g(q,\omega,p) + H(q,\omega) + h(\sigma,\omega,p)u] - \ddot{q}_r + C(\dot{q} - \dot{q}_r) + K(q - q_r) = 0 \tag{63}$$

For the specific case of the Mars ellipsled, the terms in this equation are defined as follows:

$$\frac{\partial f}{\partial \omega} = A(q) \tag{64}$$

$$\frac{\partial f}{\partial q} = \begin{pmatrix} 2\omega_1 q_1 & \omega_2 q_2 & \omega_3 q_3 \\ \omega_1 q_2 & 2\omega_2 q_2 & \omega_3 q_2 \\ \omega_1 q_3 & \omega_2 q_3 & 2\omega_3 q_3 \end{pmatrix} \tag{65}$$

$$h = [I^*]^{-1} \tag{66}$$

$$H = [I^*]^{-1}(\omega \times I^*\omega) \tag{67}$$

$$g = \frac{1}{2}\rho v^2 S_{\text{ref}} l_{\text{ref}} \begin{pmatrix} \frac{c_{l_\beta}\beta}{I_x^*} \\ \frac{c_{m_\alpha}\alpha}{I_y^*} \\ \frac{c_{n_\beta}\beta}{I_z^*} \end{pmatrix} \tag{68}$$

where S_{ref} is the vehicle reference area; l_{ref} is the reference length; and c_{l_β}, c_{m_α}, and c_{n_β} are aerodynamic coefficients. The g term contains both known and unknown parameters, and it is crucial to separate them. The most critical unknown parameter for the Mars entry problem is the atmospheric density ρ. Additionally, the aerodynamic coefficients are typically highly uncertain, and g contains both of these parameters. The controller gains are specifically designed to adapt for this lack of knowledge. The g term can be rewritten as follows:

$$g = \frac{1}{2} v^2 S_{\text{ref}} l_{\text{ref}} [I^*]^{-1} \begin{pmatrix} \beta & 0 & 0 \\ 0 & \alpha & 0 \\ 0 & 0 & \beta \end{pmatrix} \rho \begin{pmatrix} c_{l_\beta} \\ c_{m_\alpha} \\ c_{n_\beta} \end{pmatrix} \tag{69}$$

This expression can also be written as $g = GL$, where G contains the known parameters and L contains the unknown parameters. The parameters in G are true values that are known to the controller; the parameters in L consisting of the aerodynamic coefficients and atmospheric density are unknown to the controller. The density and aerodynamic coefficient uncertainties are not hard-coded into the simulation. The effect of these uncertainties is created by using a control law that completely ignores the true values and instead uses only the estimates calculated by the adaptation law for L given in Eq. (86).

$$G = \frac{1}{2} V^2 S_{\text{ref}} l_{\text{ref}} [I^*]^{-1} \begin{pmatrix} \beta & 0 & 0 \\ 0 & \alpha & 0 \\ 0 & 0 & \beta \end{pmatrix} \tag{70}$$

$$L = \rho \begin{pmatrix} c_{l_\beta} \\ c_{m_\alpha} \\ c_{n_\beta} \end{pmatrix} \tag{71}$$

An adaptive controller works well when the adaptation loop is slower than the dynamics of the system. However, for the Mars ellipsled density, it is an explicit function of altitude that changes rapidly with time. To mitigate this problem, the density, which is typically an exponential model, is separated into known and unknown vectors by expressing it as a power series in h:

$$\rho = \mathbf{f}(h)^T \boldsymbol{\Theta} \tag{72}$$

where the known vector $\mathbf{f}(h)$ and the unknown parameter vector $\boldsymbol{\Theta}$ are expressed as

$$\mathbf{f}(h) = \begin{bmatrix} 1 & h & h^2 & h^3 & h^4 \\ 1 & h & h^2 & h^3 & h^4 \\ 1 & h & h^2 & h^3 & h^4 \end{bmatrix} \tag{73}$$

$$\boldsymbol{\Theta} = \begin{bmatrix} \Theta_{11} & \Theta_{12} & \Theta_{13} & \Theta_{14} & \Theta_{15} \\ \Theta_{21} & \Theta_{22} & \Theta_{23} & \Theta_{24} & \Theta_{25} \\ \Theta_{31} & \Theta_{32} & \Theta_{33} & \Theta_{34} & \Theta_{25} \end{bmatrix} \tag{74}$$

because the density is now separated into known and unknown vectors, the terms G and L can be redefined as

$$G = \frac{1}{2} V^2 S_{\text{ref}} l_{\text{ref}} [I^*]^{-1} \begin{pmatrix} \beta & 0 & 0 \\ 0 & \alpha & 0 \\ 0 & 0 & \beta \end{pmatrix} \mathbf{f}^T(h) \tag{75}$$

$$L = \boldsymbol{\Theta} \begin{pmatrix} c_{l_\beta} \\ c_{m_\alpha} \\ c_{n_\beta} \end{pmatrix} \tag{76}$$

With expressions for all of the terms in the error dynamics equation derived, it is now possible to solve for the control law u. Note that the inertia matrix in the control law is $[I]$ and not $[I^*]$, which means that the control law has no knowledge of the true inertia value and so it uses its estimates instead:

$$u = -\left(\frac{\partial f}{\partial \omega}[I]^{-1}\right)^{-1}\left[\frac{\partial f}{\partial \omega}(GL + H) + \frac{\partial f}{\partial q}\dot{q} - \ddot{q}_r + C(\dot{q} - \dot{q}_r) + K(q - q_r)\right] = -[I]\left[GL + \frac{\partial f^{-1}}{\partial \omega}\left(\frac{\partial f}{\partial \omega}H + \frac{\partial f}{\partial q}\dot{q} - \ddot{q}_r + C(\dot{q} - \dot{q}_r) + K(q - q_r)\right)\right] \tag{77}$$

To simplify this expression, the control law is written as

$$u = -[I](GL + \Psi) \tag{78}$$

where Ψ is defined as

$$\Psi = \frac{\partial f^{-1}}{\partial \omega}\left(\frac{\partial f}{\partial \omega}H + \frac{\partial f}{\partial q}\dot{q} - \ddot{q}_r + C(\dot{q} - \dot{q}_r) + K(q - q_r)\right) \tag{79}$$

The control law in Eq. (78) requires knowledge of L and I, and so adaptive laws are developed for each. The true values of L and I are defined as L^* and I^* and their estimates are $L(t)$ and $I(t)$. Adaptation laws are developed for the difference between the true and the estimated values of each parameter and are defined as

$$\tilde{L} = L(t) - L^* \tag{80}$$

$$\tilde{I} = I(t) - I^* \tag{81}$$

The control identity is defined as $GL + \Psi + I^{-1}u = 0$. Adding and subtracting the control identity for the known and unknown parameter cases to the error dynamics equation produces

$$\ddot{e} + C\dot{e} + Ke = GL + \Psi + I^{-1}u - GL^* - \Psi - I^{*-1}u \tag{82}$$

$$\ddot{e} = -C\dot{e} - Ke + G\tilde{L} + \tilde{I}^{-1}u \tag{83}$$

With $C = k_1 + k_2$ and $K = k_1 k_2$, where k_1 and k_2 are positive scalar constants, a candidate positive-definite Lyapunov function is given

by Eq. (84). The first and second terms contain the bank-angle error and its derivative, and the third and fourth terms will yield the adaptation laws for L and $\mathcal{I}$:

$$V = \tfrac{1}{2}(\dot{e} + k_1 e)^T(\dot{e} + k_1 e) + \tfrac{1}{2}\tilde{L}^T\Gamma_1^{-1}\tilde{L} + \tfrac{1}{2}Tr[\tilde{\mathcal{I}}^T\Gamma_2^{-1}\tilde{\mathcal{I}}] \quad (84)$$

Let $\tilde{I}^{-1}$ be redefined as $\tilde{\mathcal{I}}$ for convenience of notation. The time derivative of the Lyapunov function is then given by

$$\begin{aligned}\dot{V} &= (\dot{e} + k_1 e)^T(\ddot{e} + k_1\dot{e}) + \tilde{L}^T\Gamma_1^{-1}\dot{\tilde{L}} + \mathrm{Tr}[\tilde{\mathcal{I}}^T\Gamma_2^{-1}\dot{\tilde{\mathcal{I}}}] \\ &= (\dot{e} + k_1 e)^T[-(k_1 + k_2)\dot{e} - k_1 k_2 e + G\tilde{L} + \tilde{\mathcal{I}}u + k_1\dot{e}] \\ &+ \tilde{L}^T\Gamma_1^{-1}\dot{\tilde{L}} + \mathrm{Tr}[\tilde{\mathcal{I}}^T\Gamma_2^{-1}\dot{\tilde{\mathcal{I}}}] = (\dot{e} + k_1 e)^T[-k_2\dot{e} - k_1 k_2 e + G\tilde{L} \\ &+ \tilde{\mathcal{I}}u] + \tilde{L}^T\Gamma_1^{-1}\dot{\tilde{L}} + \mathrm{Tr}[\tilde{\mathcal{I}}^T\Gamma_2^{-1}\dot{\tilde{\mathcal{I}}}] = -k_2(\dot{e} + k_1 e)^T(\dot{e} + k_1 e) \\ &+ [(\dot{e} + k_1 e)^T G\tilde{L} + \tilde{L}^T\Gamma_1^{-1}\dot{\tilde{L}}] + [(\dot{e} + k_1 e)^T\tilde{\mathcal{I}}u + \tilde{\mathcal{I}}^T\Gamma_2^{-1}\dot{\tilde{\mathcal{I}}}]\end{aligned} \quad (85)$$

for the derivative of the Lyapunov function to be negative semidefinite, the second and third terms of Eq. (85) are set to zero. This yields the following adaptive laws for L and I:

$$\dot{\tilde{L}} = -\Gamma_1 G^T(\dot{e} + k_1 e) \quad (86)$$

$$\dot{\tilde{\mathcal{I}}} = -\Gamma_2 u(\dot{e} + k_1 e)^T \quad (87)$$

Equations (86) and (87) summarize the adaptive laws to be used along with the control law in Eq. (78) to achieve the desired tracking objectives. The preceding adaptive laws ensure that the tracking errors and the parameter errors are bounded. To prove asymptotic stability of the tracking error dynamics in Eq. (83) with the control law in Eq. (78) and the adaptation laws in Eqs. (86) and (87), we use Barbalat's lemma [23], because the system is nonautonomous due to the time-dependent terms on the right-hand side of Eq. (83). Because $\dot{V} \leq 0$ and $V \geq 0$, all terms in $V \in \mathcal{L}_\infty$ (i.e., $\{e, \dot{e}, \tilde{L}, \tilde{\mathcal{I}}\} \in \mathcal{L}_\infty$). This is the case because $\dot{e} + k_1 e \in \mathcal{L}_\infty$ implies uniform boundedness of both e and $\dot{e}$. Integrating $\dot{V}$ over $[0, \infty]$, it can be shown that $\dot{e} + k_1 e \in \mathcal{L}_2 \cap \mathcal{L}_\infty$ as well. Now consider $\ddot{e}$ in Eq. (83). The reference trajectory states are bounded, and from the expression for u in Eq. (78), we conclude that $u \in \mathcal{L}_\infty$. Hence, all the terms on the right-hand side of Eq. (83) are bounded, and thus $\ddot{e} \in \mathcal{L}_\infty$. Using Barbalat's lemma, we conclude that $\dot{e} + k_1 e \to 0$ as $t \to \infty$. Using the final value theorem, we conclude that $e \to 0$ as $t \to \infty$, and hence the error converges asymptotically. This completes the proof.

To summarize, the adaptive laws for the density function coefficients and aerodynamic coefficients and for the inverse of the inertia matrix are given in Eqs. (86) and (87), respectively. The adaptation rate depends on the learning rates Γ_1 and Γ_2. Note that these control laws do not guarantee parameter estimate convergence; they can only guarantee error convergence.

VI. Numerical Simulation Results

The objective of the simulation effort is to exercise the MRAC and SAMI controllers for the Mars entry problem. Performance metrics are introduced, and the relative benefits and disadvantages of each controller are discussed in terms of the results. Each controller is evaluated in terms of trajectory-tracking performance while in the presence of uncertainties in the atmospheric density, uncertainties in the aerodynamic coefficients, and uncertainties in the vehicle inertias. Instead of introducing specific percentages of density uncertainties, density dispersions and severity are accounted for by setting the controller to have no knowledge whatsoever of the true density. This condition represents controller operation in the presence of the highest degree of uncertainty and severity, and is used for both the density and the aerodynamic coefficients. For all simulation cases, the entry-interface conditions are a velocity of 7.3 km/s, an altitude of 125 km, and an initial condition bank-angle error of 3 deg. First, several bank-angle step commands are issued to each controller to find the largest bank-angle command that can be tracked in the shortest time. These commands are then used in two cases to determine the effects of density uncertainties. In the first case, the controller uses the true density, and in the second case, the control law has no knowledge of the true density; therefore, estimates of the unknown parameter vector are used to approximate a density function throughout the entry. A third case is used to determine the effect of uncertainties in the vehicle inertias, and a fourth case is used to determine the effect of simultaneous errors in the density, aerodynamic coefficients, and vehicle inertias. Both controllers are then evaluated for trajectory-tracking performance during a complete Mars entry scenario. Results are presented first for the MRAC controller, then for the SAMI controller, and then a direct evaluation is presented.

A. MRAC

The values for the tuning parameters were selected based on the performance of the controller while tracking the aforementioned smooth-entry trajectory. The control law is given by $u = \tilde{a}_r\omega_r + \tilde{a}_\omega\omega$, where the gains $\tilde{a}_r$ and $\tilde{a}_\omega$ are adaptive. Their adaptation equations require an initial value and a learning rate. The learning rate was selected as $\Gamma = 1 \times 10^5$ to minimize the control input. The initial gain values were selected as

$$\tilde{a}_r(0) = \tilde{a}_\omega(0) = \begin{bmatrix} 1\times10^3 & 0 & 0 \\ 0 & 1\times10^3 & 0 \\ 0 & 0 & 1\times10^4 \end{bmatrix} \quad (88)$$

based on the average value of the gains throughout the simulation. It is important to point out that the basic MRAC control system developed here defines the error as $e = \omega - \omega_r$. The derivation of the adaptive laws guarantees convergence of the angular velocities, but it does not guarantee convergence of attitude error or unknown parameter estimates.

1. *Step Response for the MRAC Controller*

The largest bank-angle command chosen was from 0 to 170 deg. An angle of 170 deg corresponds to pointing the lift vector **L** nearly toward the ground. This bank angle was commanded in several time intervals; it was determined that the fastest time interval in which the ellipsled can perform this maneuver without exceeding the available control input limits is approximately 10 s. Figure 11 shows the tracking performance of the MRAC controller for a bank-angle command of 170 deg. Clearly, there is a steady-state error, because the MRAC controller guarantees convergence of the angular velocity error but not of the attitude error. Figure 12 shows the control input

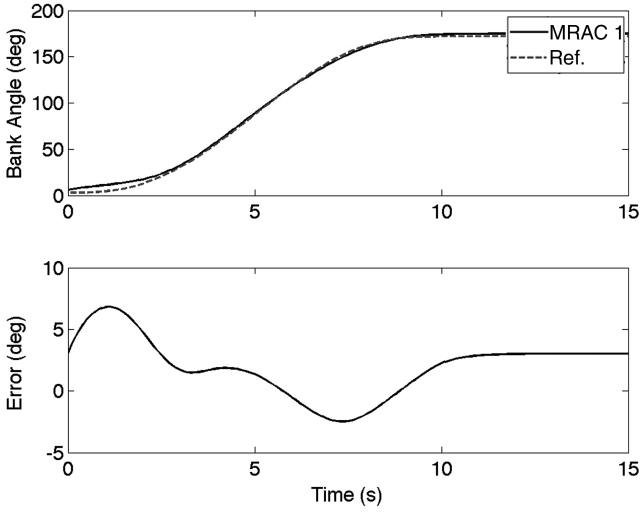

Fig. 11 MRAC maximum bank-angle command step response.

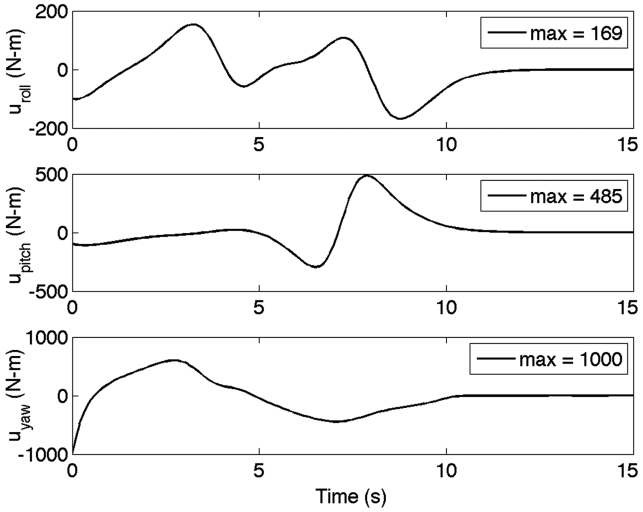

Fig. 12 MRAC maximum control inputs during step response.

required to perform this maneuver. The magnitudes of the control input signals for each axes are close to the RCS jet capabilities. Because of the large bank command of 170 deg, the yaw jets briefly exceed their limit of 849 $\mathrm{N}\cdot\mathrm{m}$ during the first second of the simulation.

2. Effects of Uncertainties on the MRAC Controller

One of the main differences between the basic MRAC and SAMI is that MRAC cannot directly estimate unknown system parameters. The MRAC gains vary with the angular velocity error, and their values are not based on attitude error convergence or on unknown parameter estimates. This means that the adaptation mechanism does not depend directly on parameter estimation errors, and so it is not possible to explicitly test the controller for a given amount of uncertainty in the system parameters. For example, making a comparison between a case with 50% density uncertainty and a case with 90% density uncertainty would only show that the controller gains reach different steady-state values after a given period of time, yet the performance of the system is approximately the same.

3. Trajectory-Tracking Performance of the MRAC Controller

Figure 13 shows that there is a steady-state error present during most of the simulation run. This is because MRAC guarantees angular velocity error convergence, but not necessarily attitude error convergence. Even though the learning rates for an MRAC controller are not difficult to tune, it is not trivial to find a set of learning rates that produce high levels of performance throughout an entire entry trajectory. Toward the end of the simulation run, a larger error can be seen. This is a result of the atmospheric density changing faster than the controller gains.

B. SAMI

Recall that SAMI adapts for unknown system parameters explicitly, but does not guarantee convergence to the true values. The unknown parameters change with time only until error convergence is achieved. The tuning parameters for this controller are selected by evaluating response performance while tracking a smooth trajectory. These parameters are the error dynamics gains C and K, the initial values for $\mathcal{I}$ and L, and the learning rates Γ_1 and Γ_2 from Eqs. (86) and (87), respectively. The error dynamics gains were selected as $C = 0.1 \cdot [1]$ and $K = 10 \cdot [1]$, where [1] is the identity matrix. The initial estimates for the inertias were selected as 80% of the true values. The initial estimates for the L vector were selected to be zero because this vector is composed of the aerodynamic coefficients and the atmospheric density function coefficients, which are all small numbers.

The learning rates were selected as $\Gamma_1 = 1 \times 10^2 \cdot [1]$ and $\Gamma_2 = 1 \times 10^{-5} \cdot [1]$. Selecting the learning rates for the SAMI controller is not trivial, because there are several possible combinations of learning rates that can work for various magnitudes of step commands. Therefore, finding the appropriate combination of learning rates for both the unknown parameter vector L and the inverse of the inertia matrix $\mathcal{I}$ requires several iterations. In general, the process consists of running several step commands for different points in the trajectory. Different step commands for various dynamic pressures are then evaluated until an appropriate combination of learning rates is obtained. Adapting for the inverse of the inertia matrix requires small learning rates because these parameters are very small. Higher learning rates cause high-frequency oscillations in the estimates, which translate into high-frequency oscillations in the control input signal. Conversely, adapting for the unknown parameter vector L requires a fast learning rate. This is because the density varies rapidly throughout the flight, and so its estimates must also change rapidly.

1. Step Response for the SAMI Controller

Figure 14 shows the commanded maneuver as well as the bank-angle error. The tracking error quickly goes to zero and satisfactory tracking is achieved in less than 10 s. Figure 15 shows that the control input is within the RCS jet limitations presented on Table 3. It was determined that the SAMI controller can track a bank angle of 170 deg in approximately 12 s without exceeding the control input limits.

2. Effects of Uncertainty in Atmospheric Density and Aerodynamic Coefficients

Figures 16 and 17 show the results for two cases. The first case (denoted by True in the figures) represents the response of the SAMI controller assuming true density values. The second case (denoted by Est.) represents the response of the SAMI controller that uses estimates of the density. Figure 16 shows that the tracking performance for both cases is similar in terms of error convergence. Figure 17 shows the control inputs required for this maneuver, with the roll and yaw signals being similar in magnitude. However, the

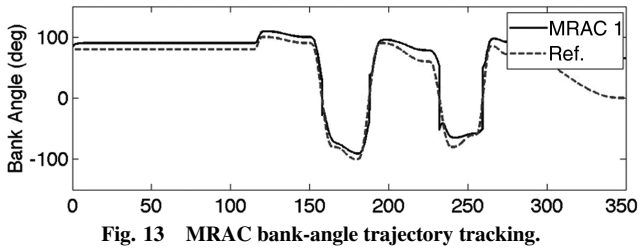

Fig. 13 MRAC bank-angle trajectory tracking.

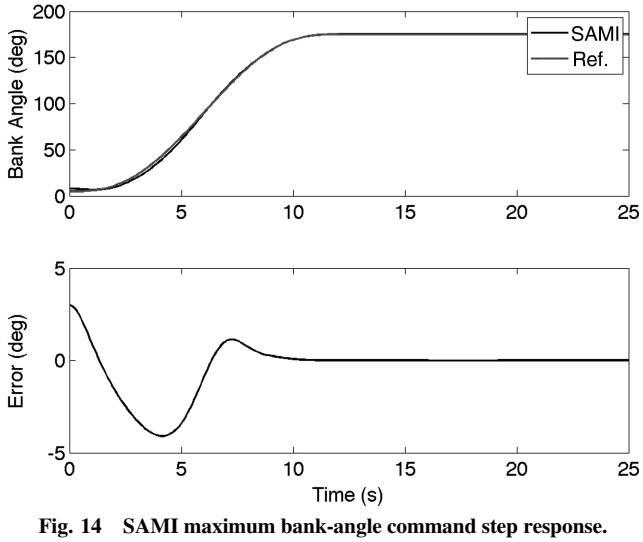

Fig. 14 SAMI maximum bank-angle command step response.

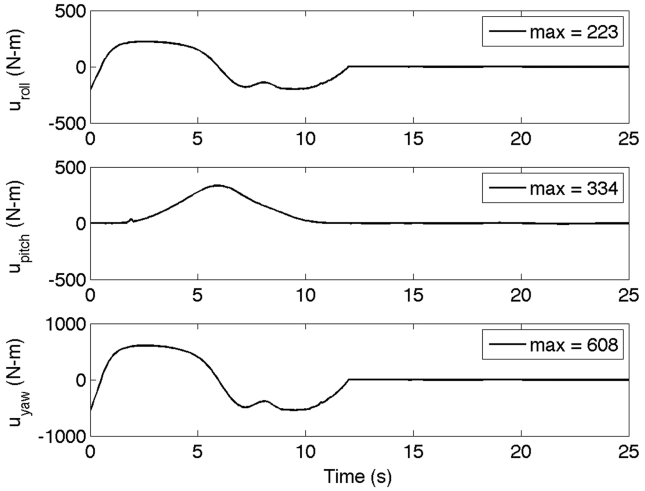

Fig. 15 SAMI maximum control inputs during step response.

pitch control input is significantly higher for this case with unknown density and aerodynamic coefficients. This is because the pitching-moment coefficient is much more sensitive to errors than the rolling and yawing coefficients, because the equations of motion were developed under the assumption that the vehicle remains trimmed in pitch throughout the trajectory.

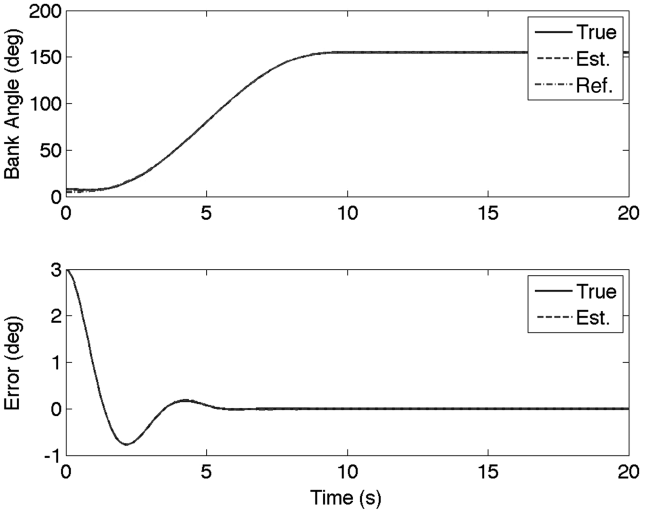

Fig. 16 SAMI bank-angle step response: uncertainties in aerodynamic coefficients and density.

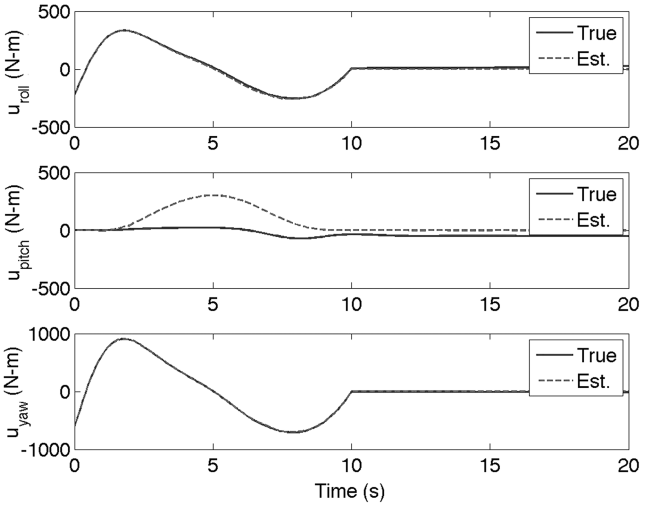

Fig. 17 SAMI control input during step response: uncertainties in aerodynamic coefficients and density.

3. *Effects of Uncertainty in the Vehicle Inertias*

As previously noted, the SAMI controller estimates the inverse of the inertia matrix $[I]^{-1}$. The simulation was run for cases in which both the true inertia values and the inertia estimates are used. Figures 18 and 19 show that the controller performs well in both cases. The bank-angle error and the control input signals are of comparable magnitudes. The main difference between the two cases is the initial oscillation in the control input signal due to the estimation of the inertias. Once the inertia values have settled, as seen in Fig. 20, the control input signal is as smooth as it is in the case in which the controller has full knowledge of the true inertias.

4. *Effects of Uncertainties in Vehicle Inertias, Aerodynamic Coefficients, and Density*

This is the demanding case of tracking a trajectory while adapting for a 10% error in the inertias, in addition to the controller having no knowledge whatsoever of the aerodynamic coefficients and density. Although unlikely, this case is useful for illustrating the limits of controller performance and shows what can be accomplished if the control limits are relaxed slightly. Figures 21–23 compare a controller that has knowledge of all parameters (True) with a controller that uses uncertain parameters (Est.). Both controllers were simulated with an initial bank-angle error of 3 deg. As expected,

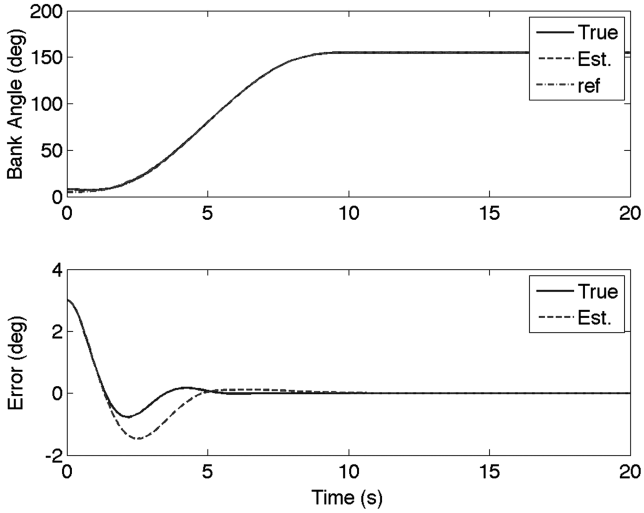

Fig. 18 SAMI bank-angle step response: uncertainties in inertias.

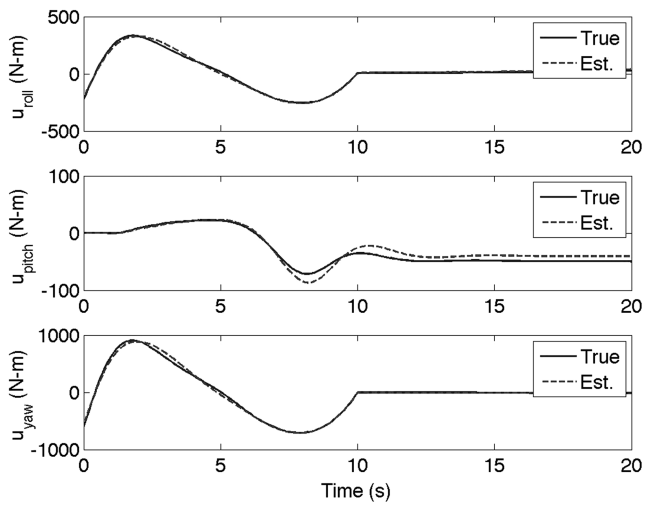

Fig. 19 SAMI control inputs during step response: uncertainties in inertias.

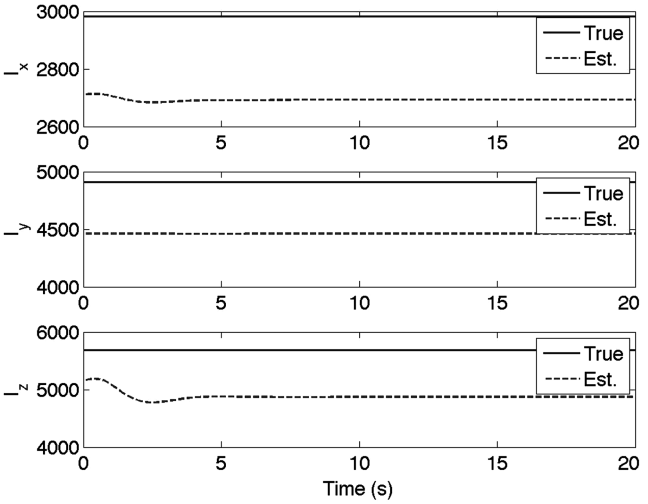

Fig. 20 SAMI true and estimated inertias during step response.

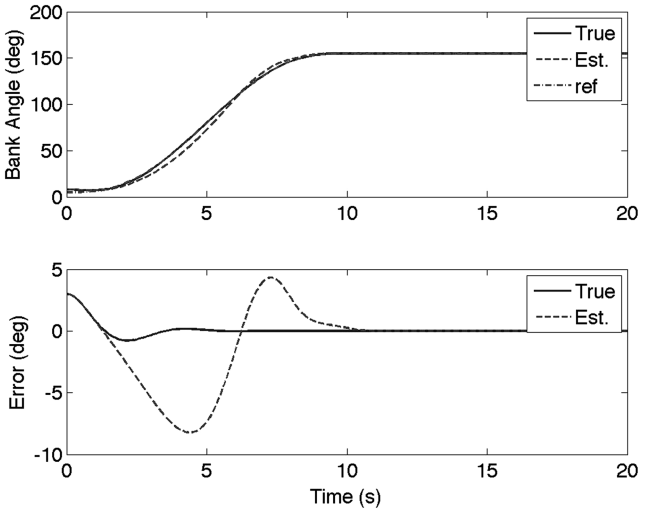

Fig. 21 SAMI bank-angle step response: uncertainties in inertias, aerodynamic coefficients, and density.

the error converges faster for the controller that has full knowledge of all parameters. The combination of pitch and roll jets exceeds the limits in Table 3, due to the large near-simultaneous errors, but it is important to note that when the pitch jets fire, the roll jets are close to

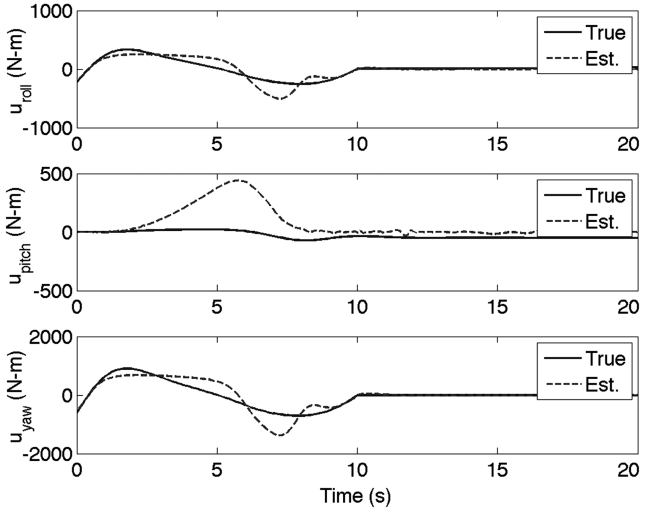

Fig. 22 SAMI control inputs during step response: uncertainties in inertias, aerodynamic coefficients, and density.

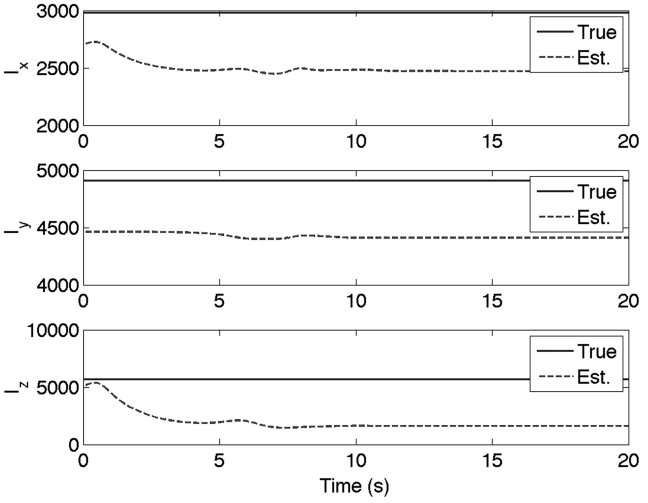

Fig. 23 SAMI true and estimated inertias during step response: uncertainties in inertias, aerodynamic coefficients, and density.

zero, and vice versa. Thus, adding the values for all time instances does not exceed the value of firing all six sets at one time. Figure 23 shows the time history of the estimates of the vehicle inertias. These values do not converge to the true values, but they settle to a constant value as soon as bank-angle error convergence is achieved. The results of this case demonstrate that the SAMI controller can perform well without precise knowledge of the vehicle inertias, aerodynamic coefficients, or atmospheric density, but this good performance comes with a penalty of increased control.

5. Trajectory Tracking for the SAMI Controller

Figures 24–29 present SAMI control-system tracking performance during an entry trajectory. Figure 24 shows rapid convergence from the 3-deg initial error in bank angle, yet there is an additional small error at approximately 260 s. This terminal error is due to the steep command that the controller must track at that particular time. Figure 25 shows the control input required to follow the trajectory and the maximum controls. The yaw control input exceeds the limits by approximately 100 N at approximately 260 s. This is due once again to the very aggressive maneuver being tracked. Figure 26 shows that the angular velocities are all within limits. Figure 27 shows that inertias I_x and I_z take some time to converge to a constant value, whereas I_y is nearly constant most of the time. This is because the vehicle is stable in pitch, and the controller is primarily tracking maneuvers that involve rolling and yawing motions.

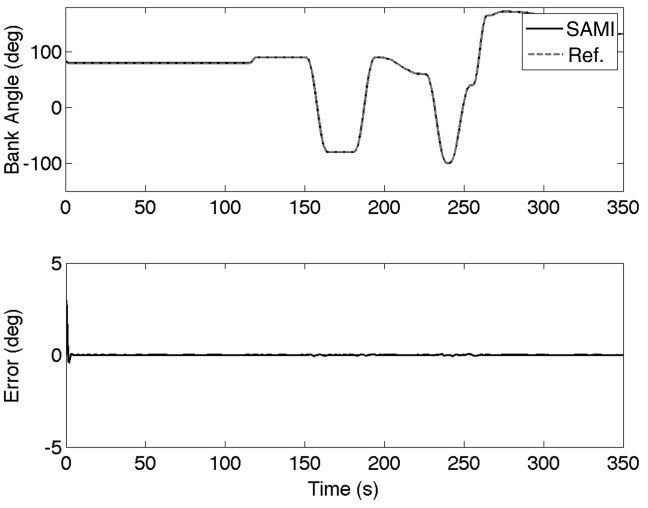

Fig. 24 SAMI bank-angle response during trajectory tracking.

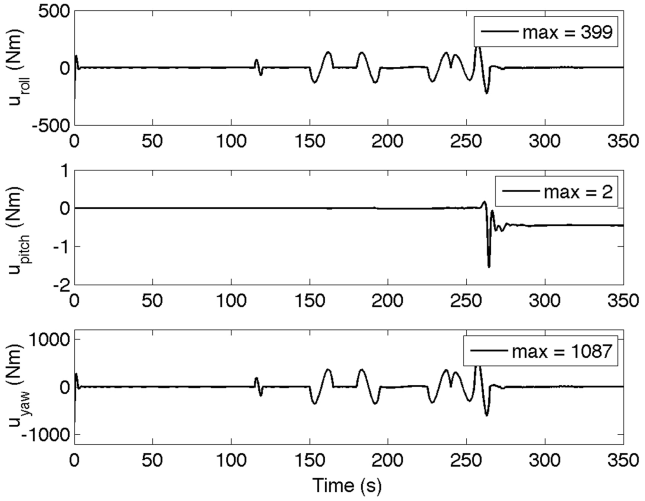

Fig. 25 SAMI control inputs during trajectory tracking.

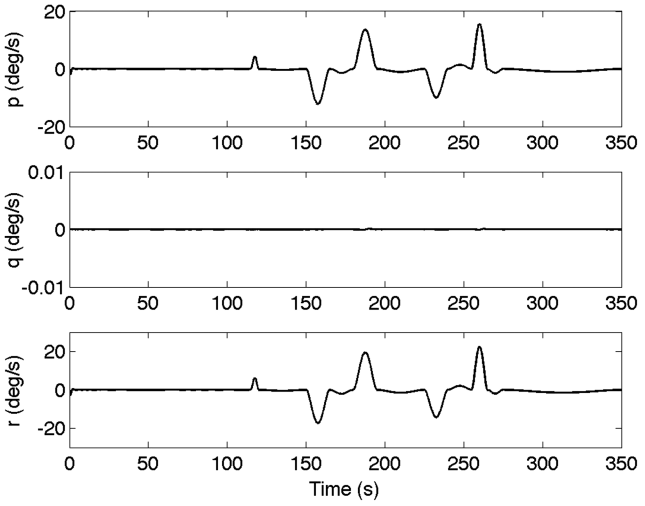

Fig. 26 SAMI angular velocity during trajectory tracking.

Recall that the entry-interface conditions include a velocity of 7.3 km/s and an altitude of 125 km. Figure 28 shows the downrange and altitude trajectories with respect to the surface of the planet and the velocity. Note that velocity is reduced as soon as the dynamic pressure peaks, at which time altitude rate also decreases. This effect can also be seen in Fig. 29, in which the flight-path angle changes

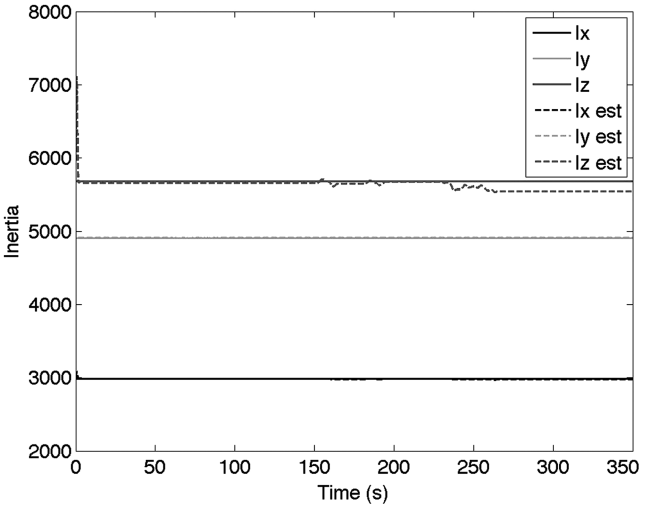

Fig. 27 SAMI true and estimated inertias during trajectory tracking.

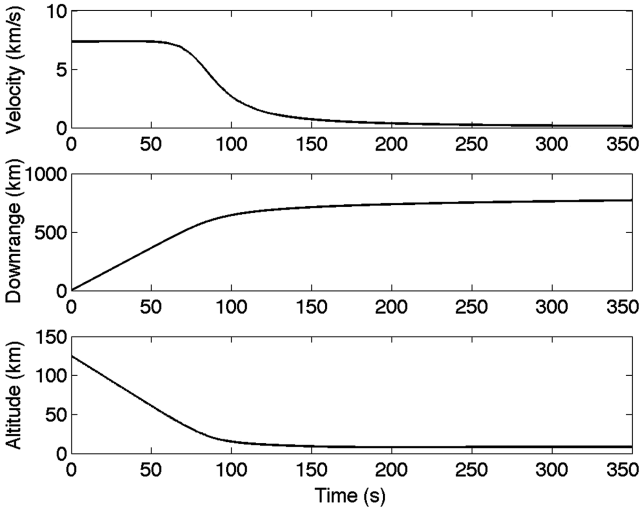

Fig. 28 SAMI inertial velocity, downrange, and altitude during trajectory tracking.

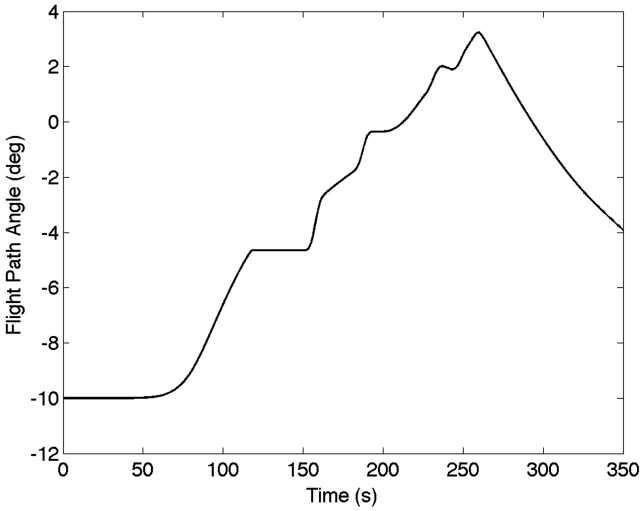

Fig. 29 SAMI flight-path angle during trajectory tracking.

from a negative value to a positive value. This sign change occurs when the dynamic pressure peaks or soon thereafter, when the aerodynamic forces have a larger magnitude than the gravity force.

Based upon these results, SAMI is judged to be capable of tracking a demanding entry trajectory. The controller is robust enough to

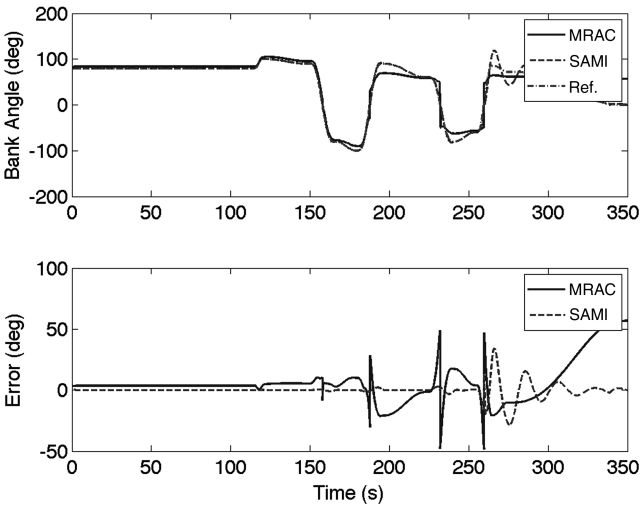

Fig. 30 MRAC and SAMI bank-angle step response.

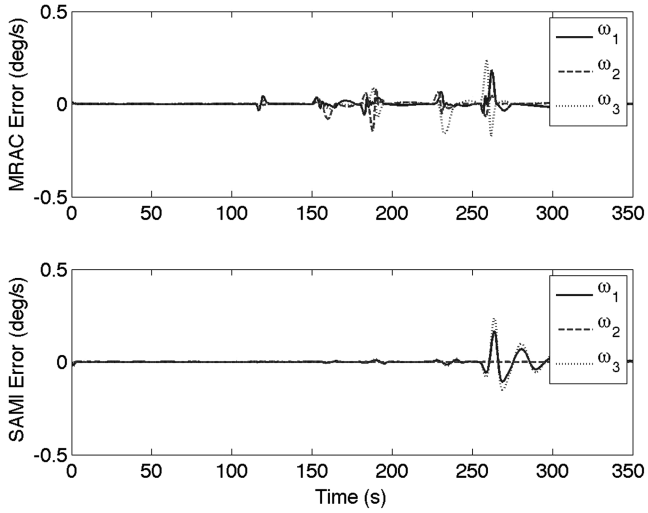

Fig. 31 MRAC and SAMI angular velocity during step response.

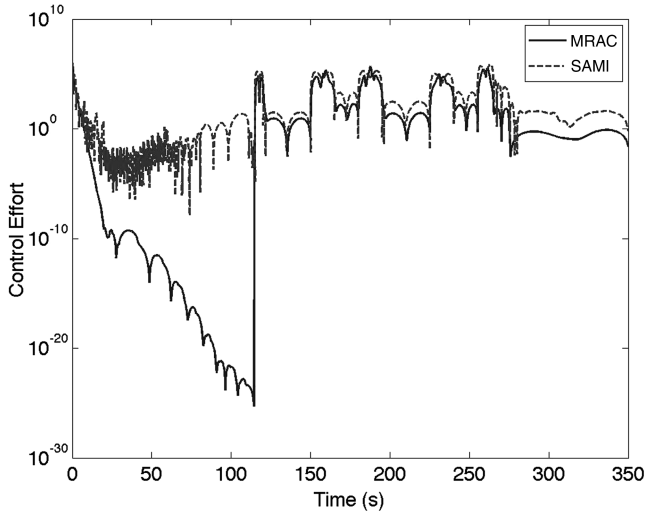

Fig. 32 MRAC and SAMI control effort during entry trajectory.

operate without knowledge of atmospheric density, as well as with incorrect values of vehicle inertias and aerodynamic properties.

C. Direct Comparison of MRAC and SAMI

This section highlights and contrasts the performance of the MRAC and SAMI adaptive control systems for the same entry trajectory scenario. Figures 30 and 31 illustrate the performance of both controllers over the same complete entry trajectory. Although Fig. 30 shows that MRAC has a significant steady-state error after every bank command, Fig. 31 demonstrates that both controllers can handle the same drastic changes in angular velocity to achieve each bank command in a similar form. The control effort for this trajectory, defined as $u^T u$, is plotted in Fig. 32. Another useful metric is the integral of $\|u\|$ over time, which is proportional to fuel consumption. This is shown in Fig. 33.

VII. Conclusions

For the Mars entry control problem studied in this paper, each controller performed well with uncertainties in the environment and vehicle model. Model reference adaptive control was capable of tracking bank-angle commands up to 170 deg in approximately 10 s, provided the trajectory is smooth. It was also possible to tune the learning rates and other parameters to obtain acceptable tracking performance during an entire entry trajectory. Because it specifically adapts for the lack of knowledge of atmospheric density, vehicle

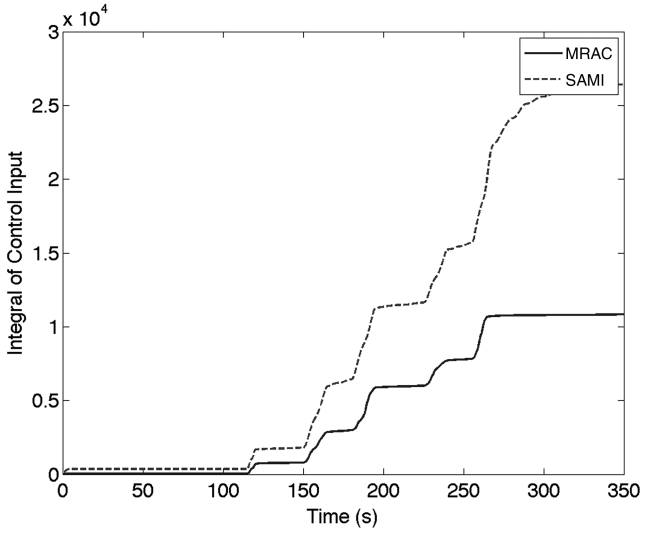

Fig. 33 MRAC and SAMI integral of control input during entry trajectory.

aerodynamic coefficients, and vehicle inertias, the tracking error of the structured adaptive model inversion controller converged to zero rapidly. However, the structured adaptive model inversion controller requires more control energy than the model reference adaptive controller to track the same reference trajectory.

The model reference adaptive controller is straightforward to design and implement because it is not sensitive to the gain values or learning rates. The structured adaptive model inversion controller requires a degree of skill and experience to design because of the dynamical structuring and modeling aspects. Tuning of the structured adaptive model inversion controller can be demanding because of the sensitivity of the learning rates to atmospheric density and vehicle inertias. Because atmospheric density changes rapidly and the control law is an explicit function of the vehicle inertias, the controller is sensitive with respect to how fast these values can be estimated. Which of the two model reference adaptive controllers is most suitable for a particular Mars entry application depends upon the tradeoff between level of performance and higher control effort and the level of difficulty in the synthesis and implementation efforts.

Acknowledgments

The authors wish to acknowledge the support of NASA Johnson Space Center under award no. C06-00295. The technical monitor is Mark Hammerschmidt. The authors would like to thank Alan Strahan and David Kanipe for their many comments and suggestions. Any opinions, findings, and conclusions or recommendations expressed in this material are those of the authors and do not necessarily reflect the views of the National Aeronautics and Space Administration. The authors would also like to thank Maruthi R. Akella of the University of Texas at Austin and Kamesh Subbarao of the University of Texas at Arlington for many insightful discussions regarding this work. Finally, the authors thank the Associate Editor and reviewers for providing many suggestions that improved the manuscript.

References

[1] Graves, C., "Entry Configurations and Performance Comparisons for the Mars Smart Lander," Proceedings of the AIAA Guidance, Navigation, and Control Conference and Exhibit, Monterey, CA, Aug. 2002.

[2] Kass, D. M., Schofield, J. T., Michaels, T. I., Rafkin, S. C. R., Richardson, M. I., and Toigo, A. D., "Analysis of Atmospheric Mesoscale Models for Entry, Descent, and Landing," *Journal of Geophysical Research: Planets*, Vol. 108, No. E12, Dec. 2003, Paper 8090. doi:10.1029/2003JE002065

[3] Seiff, A., and Kirk, D., "Structure of the Atmosphere of Mars at Summer

Mid-Latitudes," *Journal of Geophysical Research*, Vol. 82, No. 28, Sept. 1977, pp. 4364–4378. doi:10.1029/JS082i028p04364

[4] Hull, N. J., Shierman, Ghandi M., Oppenheimer, J., Ward, D., and Doman, D., "Integrated Adaptive Guidance and Control for Re-Entry Vehicles with Flight-Test Results," *Journal of Guidance, Control, and Dynamics*, Vol. 27, No. 6, Nov.–Dec. 2004, pp. 975–988. doi:10.2514/1.10344

[5] Graybeal, S., and Kranzusch, K., "Entry Abort Determination Using Nonadaptive Neural Network for Mars Precision Landers," AIAA Guidance, Navigation, and Control Conference and Exhibit, San Francisco, AIAA Paper 2005-6437, Aug. 2005.

[6] Desai, P., and Knocke, P., "Mars Exploration Rovers Entry, Descent, and Landing Trajectory Analysis," AIAA/AAS Astrodynamics Specialist Conference and Exhibit, Providence, RI, AIAA Paper 2004-5092, Aug. 2004.

[7] Wong, E., and Masciarelli, J., "Autonomous Guidance and Control Design for Hazard Avoidance and Safe Landing on Mars," AIAA Atmospheric Flight Mechanics Conference and Exhibit, Monterey, CA, AIAA Paper 2002-4619, Aug. 2002.

[8] Narendra, K., and Annaswamy, A., *Stable Adaptive Systems*, Dover, Mineola, NY, 2005.

[9] Subbarao, K., "Structured Adaptive Model Inversion: Theory and Applications to Trajectory Tracking for Nonlinear Dynamical Systems," Ph.D. Dissertation, Aerospace Engineering, Texas A&M Univ., College Station, TX, 2001.

[10] Duvall, A., Justus, C., and Johnson, D., "Mars Global Reference Atmosphere Model and Database for Mission Design," NASA Marshall Space Flight Center, Huntsville, AL, 2001.

[11] Seiff, A., "Mars Atmospheric Winds Indicated by Motion of the Viking Landers During Parachute Descent," *Journal of Geophysical Research*, Vol. 98, No. E4, Apr. 1993, pp. 7461–7474. doi:10.1029/92JE02738

[12] Lemmon, M., Renno, N., Ferri, F., and Smith, P., "Dust Devils as Observed by Mars Pathfinder," *Journal of Geophysical Research*, Vol. 108, No. E12, Dec. 2003, pp. 7-1–7-10. doi:10.1029/2000JE001421

[13] Golombek, M. P., Grant, J. A., Parker, T. J., Kass, D. M., Crisp, J. A., Squyres, S. W., et al., "Selection of the Mars Exploration Rover Landing Sites," *Journal of Geophysical Research: Planets*, Vol. 108, No. E12, Dec. 2003, Paper 8072. doi:10.1029/2003JE002074

[14] Ives, D., Carman, G., and Geller, D., "Apollo-Derived Mars Precision Lander Guidance," AIAA Atmospheric Flight Mechanics Conference and Exhibit, AIAA Paper 1998-4570, 1998.

[15] Mendeck, G., and Carman, G., "Guidance Design For Mars Smart Landers Using The Entry Terminal Point Controller," AIAA Atmospheric Flight Mechanics Conference and Exhibit, AIAA Paper 2002-4502, 2002.

[16] Dutton, K., "Optimal Control Theory Determination of Feasible Return-to-Launch-Site Aborts for the HL-20 Personnel Launch System Vehicle," NASA TR 3449, July 1994.

[17] Read, P., Collins, M., Forget, F., Fournier, R., Hourdin, F., Lewis, S. R., Talagrand, O., Taylor, F. W., and Thomas, N. P. J., "A GCM Climate Database for Mars: For Mission Planning and for Scientific Studies," *Advances in Space Research*, Vol. 19, No. 8, 1997, pp. 1213–1222. doi:10.1016/S0273-1177(97)00272-X

[18] Spencer, D. A., and Braun, R. D., "Mars Pathfinder Atmospheric Entry: Trajectory Design and Dispersion Analysis," *Journal of Spacecraft and Rockets*, Vol. 33, No. 5, 1996, pp. 670–676.

[19] B. G. Drake (ed.), "Reference Mission Version 3.0 Addendum to the Human Exploration of Mars: The Reference Mission of the NASA Mars Exploration Study Team," NASA Johnson Space Center SP-6107-ADD, Houston, TX, June 1998.

[20] Astrom, K., and Wittenmark, B., *Adaptive Control*, 2nd ed., Prentice–Hall, Upper Saddle River, NJ, 1994.

[21] Bhattacharya, S., and Chapellat, L., *Robust Control: The Parametric Approach*, Prentice–Hall, Upper Saddle River, NJ, 1995.

[22] Hanaway, J., and Moorehead, R. W., "Space Shuttle Avionics System," NASA SP-504, Jan. 1989.

[23] Slotine, J., and Li, W., *Applied Nonlinear Control*, Prentice–Hall, Upper Saddle River, NJ, 1991.

[24] Iannou, P. A., and Sun, J., *Stable and Robust Adaptive Control*, Prentice–Hall, Upper Saddle River, NJ, 1995.

[25] Tandale, M. D., and Valasek, J., "Adaptive Dynamic Inversion Control with Actuator Saturation Constraints Applied to Tracking Spacecraft Maneuvers," *Journal of the Astronautical Sciences*, Vol. 52, No. 4, Oct.–Dec. 2005, pp. 517–530.

[26] Tandale, M., and Valasek, J., "Fault Tolerant Structured Model Inversion Control," *Journal of Guidance, Control, and Dynamics*, Vol. 29, No. 3, June 2006, pp. 635–642. doi:10.2514/1.15244

[27] Akella, M. R., "Structured Adaptive Model Control: Theory and Applications to Trajectory Tracking in Aerospace Systems," Ph.D. Dissertation, Aerospace Engineering, Texas A&M Univ., College Station, TX, 1999.

[28] Shaub, H., Akella, M. R., and Junkins, J. L., "Adaptive Control of Nonlinear Attitude Motions Realizing Linear Closed-Loop Dynamics," *Proceedings of the 1999 American Control Conference*, American Automatic Control Council, Evanston, IL, 1999, pp. 1563–1567.

[29] Junkins, J., Subbarao, K., and Steinberg, M., "Structured Adaptive Model Inversion Applied to Tracking Aggressive Aircraft Maneuvers," AIAA Guidance, Navigation, and Control Conference and Exhibit, AIAA Paper 2001-4019, 2001.

[30] Shaub, H., and Junkins, J., *Analytical Mechanics of Space Systems*, AIAA, Reston, VA, 2003.